



Science & Technology
Facilities Council

Technical Report
RAL-TR-2013-014

SCARF Annual Report 2012-2013

D Ross (ed)

December 2013

©2013 Science and Technology Facilities Council



This work is licensed under a [Creative Commons Attribution 3.0 Unported License](https://creativecommons.org/licenses/by/3.0/).

Enquiries concerning this report should be addressed to:

RAL Library
STFC Rutherford Appleton Laboratory
Harwell Oxford
Didcot
OX11 0QX

Tel: +44(0)1235 445384
Fax: +44(0)1235 446403
email: libraryral@stfc.ac.uk

Science and Technology Facilities Council reports are available online at: <http://epubs.stfc.ac.uk>

ISSN 1358-6254

Neither the Council nor the Laboratory accept any responsibility for loss or damage arising from the use of information contained in any of their reports or in any communication about their tests or investigations.



Science & Technology Facilities Council

SCARF Annual Report 2012-2013

Version: 1.2

Date: 10/12/2013

Edited by Derek Ross (derek.ross@stfc.ac.uk) 01235 445651

Content written by the respective authors

Date	Revision	Changes
27/09/13	1.0	Initial document
16/10/13	1.1	Scientific Contributions added
6/12/13	1.2	Layout adjustments

Abstract

Annual Report on the Usage and Scientific Impact of the SCARF Service

Dissemination

This is a public document

Contents

1. SCARF Service	5
1.1 SCARF Usage by Department	5
1.2 SCARF Availability	6
1.3 SCARF Developments 2012-13	7
1.4 Future Development	7
1.5 Help and Support	7
2. Publications and Presentations	8
2.1 Publications	8
2.2 Presentations	8
3. Science Highlights	9
3.1 C. Poulsen (RAL Space)	9
3.1.1 Cloud properties for Climate from AATSR Satellite data.	9
3.2 R. J. Dance, N. C. Woolsey, (York Plasma Institute, Department of Physics, University of York), A. P. L. Robinson, (STFC CLF)	11
3.2.1 Hybrid-PIC simulation of relativistic electron beams in solid density targets	11
3.3 A. Miceli, R. Senesi (University of Rome Tor Vergata), G. Gorini (University of Milan Bicocca), C. Andreani (University of Rome Tor Vergata)	14
3.3.1 Improving multiple prompt gamma ray analysis technique	14
3.3.2 Localization of inclusions in multiple PGGA	14
3.3.3 PGGA with neutron time of flight	15
3.4 V. Losasso (STFC Scientific Computing)	16
3.4.1 Computational studies of EGFR extracellular and intracellular domains	16
3.5 B. Pine, H. Smith, R. Williamson (ISIS)	18
3.5.1 Code Development for the ISIS Synchrotron Group	18
3.6 H. Loeffler (STFC Scientific Computing)	20
3.6.1 Free energy simulations of protein–ligand complexes and automatic setup tool development	20
3.7 A.P.L.Robinson, R.M.G.M.Trines, R.H.H.Scott, and P.A.Norreys (STFC CLF)	21
3.7.1 Fast Electron Transport	21
3.7.2 Fast Electron Generation	22
3.7.3 Brillouin amplification	22
3.7.4 High-harmonic generation in oblique laser-plasma interactions	23
3.7.5 CLF User Support	24
3.8 G. Graziano (University College London), F. Fernandez-Alonso (ISIS), A. Michaelides (University College London)	26
3.8.1 Towards a better understanding of the role of van der Waals interactions on adsorption: hydrogen on layered materials	26
3.9 G. Graziano (University College London), M. J. Gutmann (ISIS), J. Klimeš (University of Vienna), A. Michaelides (University College London), F. Fernandez-Alonso (ISIS)	28
3.9.1 Anisotropic Displacement Parameters and Diffuse Scattering in Soft Layered Materials: The Case of Graphite	28
3.10 S. Parker (ISIS), S. Deledda (Institute for Energy Technology, Norway)	32
3.10.1 Periodic-DFT of a Disordered System: $Mg_2(FeH_6)_{0.5}(CoH_5)_{0.5}$	32

3.11 L. Bernasconi, R. Webster, S. Tomic, B. Montanari and N. M. Harrison (STFC Scientific Computing)	36
3.11.1 Electronic excitations and photo-induced dynamics in extended systems	36
3.12 D. Jochym, S. Sturniolo, and K. Refson (STFC Scientific Computing)	37
3.12.1 Ferroelectric Properties of Croconic Acid	37
3.13 B. Montanari and N. M. Harrison (STFC Scientific Computing)	38
3.13.1 Surveying Defects in Graphene	38
3.14 K. Refson (STFC Scientific Computing) and M. Gutmann (ISIS)	39
3.14.1 Neutron diffuse scattering study of CaTiSiO ₅	39
3.15 S. Mukhopadhyay (ISIS)	40
3.15.1 Investigation on Vibrational Modes of Croconic Acid using Inelastic Neutron Scattering	40
3.16 C.W. Yong (STFC Scientific Computing) and R. Strange (University of Liverpool)	42
3.16.1 Molecular dynamics of a ‘tethered’ cytochrome-cupredoxin electron transfer complex	42
4. APPENDIX: SCARF Hardware Details	44
5. APPENDIX: Index of Figures	44
6. APPENDIX: Publications and Presentations	47
7. APPENDIX: SCARF Queue Usage 2011-12	50
7.1 General SCARF Queue	50
7.2 SCARF-Lexicon1 and Lexicon2 Queues	51
7.3 SCARF-IBIS	52
7.4 SCARF Total Power draw (amps)	52
7.5 Filesystem Usage	53
7.6 Networking	53
8. APPENDIX: SCARF Developments	56
8.1 Technical Developments	56
8.2 Application Stack	56
8.3 Staff Movements	56

1. SCARF SERVICE

SCARF is a High Performance Cluster for STFC staff, Facilities (ISIS, DIAMOND, CLF) and their users. The SCARF Service was started in 2004 and has been upgraded year on year and now represents a significant capital investment in High Performance Computing. Overall SCARF now has over 3500 CPU cores, 10TB memory and 100TB of disk space (Details in Appendix 1).

This report covers the year 2012-13 and outlines the research that SCARF has enabled.

1.1 SCARF Usage by Department

Each time a researcher uses the SCARF service the CPU time used is recorded. In total over 356,000 jobs, using 8.3M CPU hours, were submitted to SCARF during 2012-13.

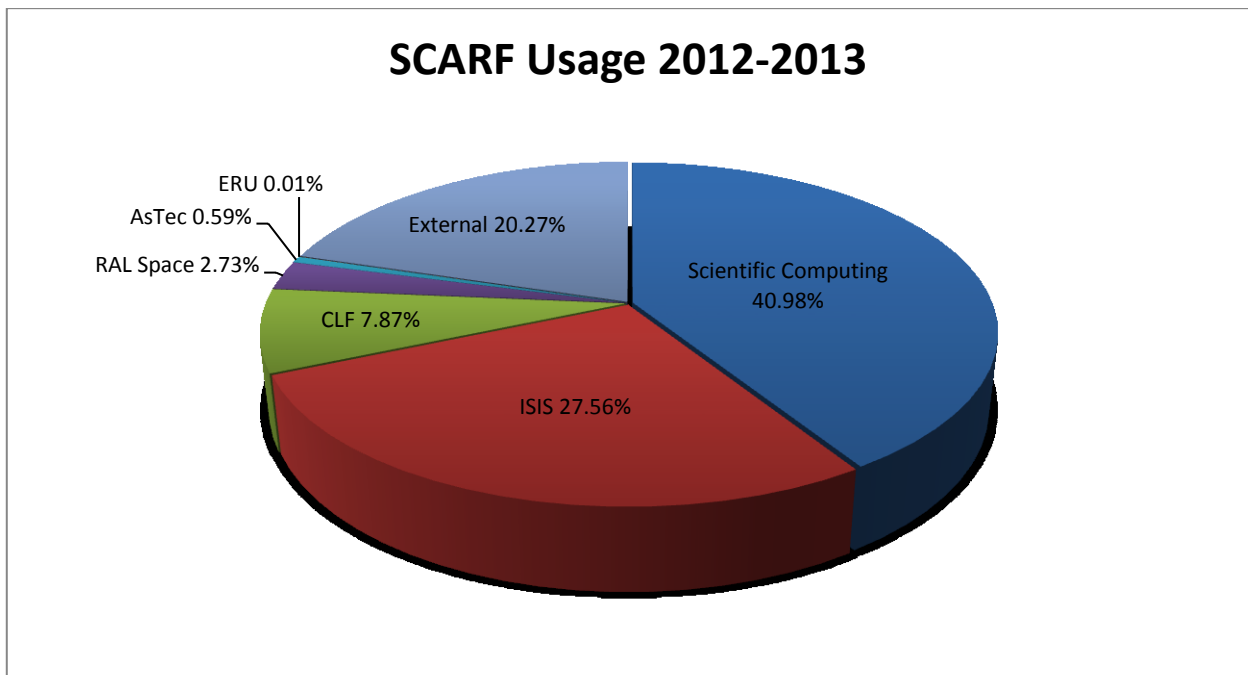


Figure 1: Pie chart showing percentage usage of the SCARF service by department

It is clear from the usage chart that ISIS and Scientific Computing are the largest users of SCARF. The External category measures the usage from STFC collaborations with York University, Bath University and the University of Strathclyde.

Dept	2012-13			2011-12			2010-11		
	Active Users	CPU hrs	%	Active Users	CPU hrs	%	Active Users	CPU hrs	%
SCD	27	3432184.71	41.0	27	2156538.5	27.4	24	2194293.0	35.9
ISIS	17	2200465.95	26.3	17	1895822.3	24.0	19	1357940.5	22.2
External	23	1697806.08	20.3	6	2571711.1	32.6	7	1471784.9	24.1
CLF	23	1099791.25	13.1	13	1086765.3	13.8	7	908121.6	14.9
ISIS_IBIS	5	107783.83	1.3	8	136678.1	1.7	5	104702.8	1.7
PPD	0	0.0	0.0	1	436.8	0.0	1	44299.4	0.7
DIAMOND	0	0.0	0.0	3	45814.3	0.6	3	26503.5	0.4
FBR	0	0.0	0.0	0	0.0	0.0	1	587.3	0.0
ASTEC	7	48549.59	0.6	0	0.0	0.0	2	0.6	0.0
RAL Space	2	215804.818	2.6	0	0.0	0.0	1	2.2	0.0
TECHNOLOGY	0	0.0	0.0	0	0.0	0.0	1	1577.2	0.0
Totals	100	8375330.95	100	75	7893766.3	100.0	71	6109811.8	100.0

Figure 2: Table displaying detailed usage from 2012-13 comparing with 2011-12 and 2010-11

A significant amount of computational resource has been used on SCARF; section 3 highlights some of the scientific achievements that have been enabled.

1.2 SCARF Availability

The most significant events impacting on availability were the two power outages in November 2012. Planned downtimes were held in January and July.

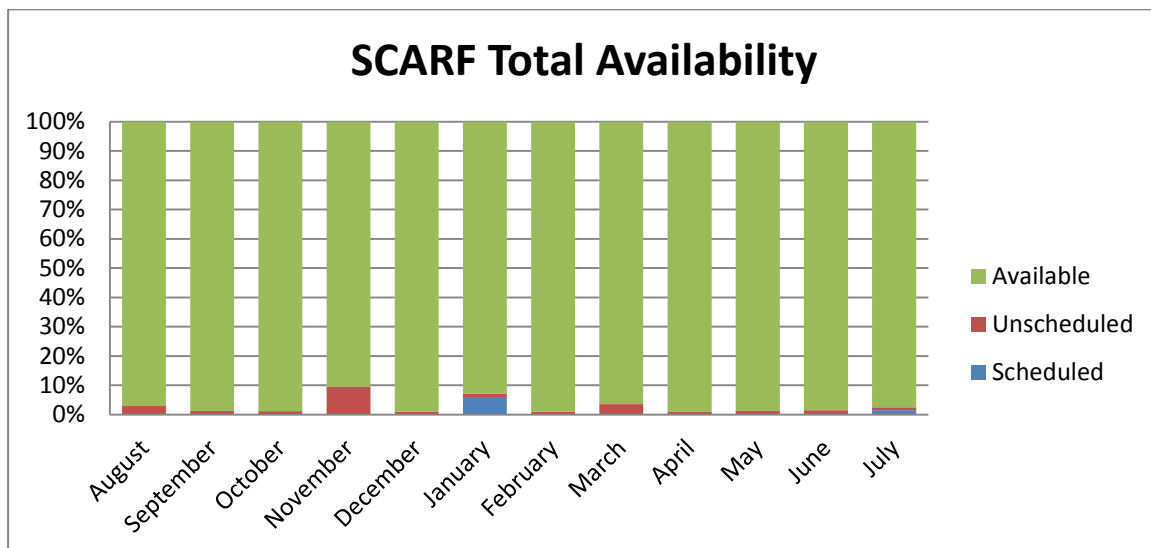


Figure 3: Availability for SCARF

As can be seen in the table below, the oldest hardware is the least available, supporting the yearly refresh cycle.

Year Purchased	Compute node Availability 2012-13	Compute node Availability 2011-12	Compute node Availability 2010-11
2008	91.2%	97.9%	98.6%
2009	99.3%	99.2%	99.8%
2010	99.1	99.9%	99.7%
2011	98.9	99.7%	100.00% (3 Months)
2012	98.9	99.9% (5 Months)	N/A
2013	100% (3 months)	N/A	N/A

Figure 4: Availability vs. Year Purchased

1.3 SCARF Developments 2012-13

Major SCARF Developments are listed below. A more detailed list can be found in Appendix 5

- New capacity added
 - 576 Intel E5-2660 CPU cores for general use went into production in June 2013
 - 512 Intel E5-2660 CPU cores for general use purchased by ISIS went into production in June 2013
 - 256 Intel E5-2660 CPU cores for CLF Lexicon went into production in June 2013

1.4 Future Development

SCARF 2014 Hardware Upgrade

- Storage Upgrade
- Service node upgrade
- Compute upgrade

Work is also on-going on a number of services to make it easier for users to submit jobs and transfer files.

1.5 Help and Support

For any queries concerning the SCARF service please email the SCARF Helpdesk; scarf@hpc-support.rl.ac.uk

2. PUBLICATIONS AND PRESENTATIONS

2.1 Publications

A list of publications is given in Appendix 3. A way of estimating the impact that SCARF has had is to analyse the Journal Impact Factor using the Journal Citation Reports published by Thomson Reuters (2012). The average Impact Factor for Journals published as a result of using SCARF is 6.8. This compares to a median impact factor across all 8424 journals of 1.352. This is a simplistic analysis but demonstrates that the science done on SCARF is having a significant impact.

2.2 Presentations

Scientists have presented their work at 12 international conferences (Appendix 3). This helps to demonstrate that the science enabled by SCARF is world class.

3. SCIENCE HIGHLIGHTS

3.1 C. Poulsen (RAL Space)

3.1.1 *Cloud properties for Climate from AATSR Satellite data.*

Over the past year the SCARF facility has been used to process cloud parameters from the AATSR (Along Track Scanning radiometer) satellite instrument for the ESA (European Space Agency) Climate Change Initiative (CCI) [1] program.

Climate change is arguably the greatest environmental challenge facing us in the twenty-first century. Its importance has been recognised in reports from the Intergovernmental Panel on Climate Change (IPCC) and from the United Nations Framework Convention on Climate Change (UNFCCC). Observations from space provide unique information that greatly assists in the successful understanding and management of climate change. The ESA CCI program aim is to produce well understood and reliable data sets in order to understand the effects of climate change.

The AATSR instrument the precursors ATSR-2 and follow on instruments SLSTR (Sea and Land Surface Temperature Radiometer) have a long history at RAL with RAL Space being involved in the design, build and calibration of the instruments. The excellent calibration and long-time series of the instrument makes it well suited for monitoring the properties of clouds and aerosols over a long time period.

The algorithm used to process the data is the ORAC (Optimal Retrieval of Aerosol and Cloud) algorithm (Poulsen et al. 2012) is an optimal estimation retrieval that can be used to determine both aerosol and cloud properties from visible/infrared satellite radiometers. In the case of cloud retrievals the algorithm fits radiances computed from LUTs created from DIScrete Ordinate Radiative Transfer (DISORT) to the TOA signal measured by the satellite by varying the cloud optical depth, effective radius cloud top pressure, phase and surface temperature simultaneously. The result is a radiatively consistent set of cloud properties. The cloud retrieval has thus far been applied to ATSR-2 and AATSR, as well as SEVIRI and AVHRR and MODIS. The optimal estimation (OE) framework of ORAC provides key advantages: the ability to include prior knowledge of the retrieved quantities is inbuilt into the method. This is particularly valuable for constraining the retrieval of surface temperature and comprehensive error propagation, allowing measurement error, forward model error (due to approximations and assumptions which must be made in the modelling to TOA radiance) and uncertainties in a priori knowledge to be combined to give a rigorous estimate of the uncertainty on retrieved values on a pixel by pixel basis.

Running the code on SCARF is complex as it involves reading in large satellite data sets and many auxiliary data sets. The processing has benefited from the SCARF facility linking with the satellite and meteorological data sets on the NEODC. The figure below shows an example of the products which have been processed on SCARF, from left to right the images show a false colour image of the clouds as viewed by the visible channels on the AATSR satellite. The cloud top height (CTH) optical depth (i.e thickness of the cloud) and effective radius of the particles visible at the top of the cloud. How these cloud properties vary over time and location is critical to understand the complex feedback mechanisms associated with climate change.

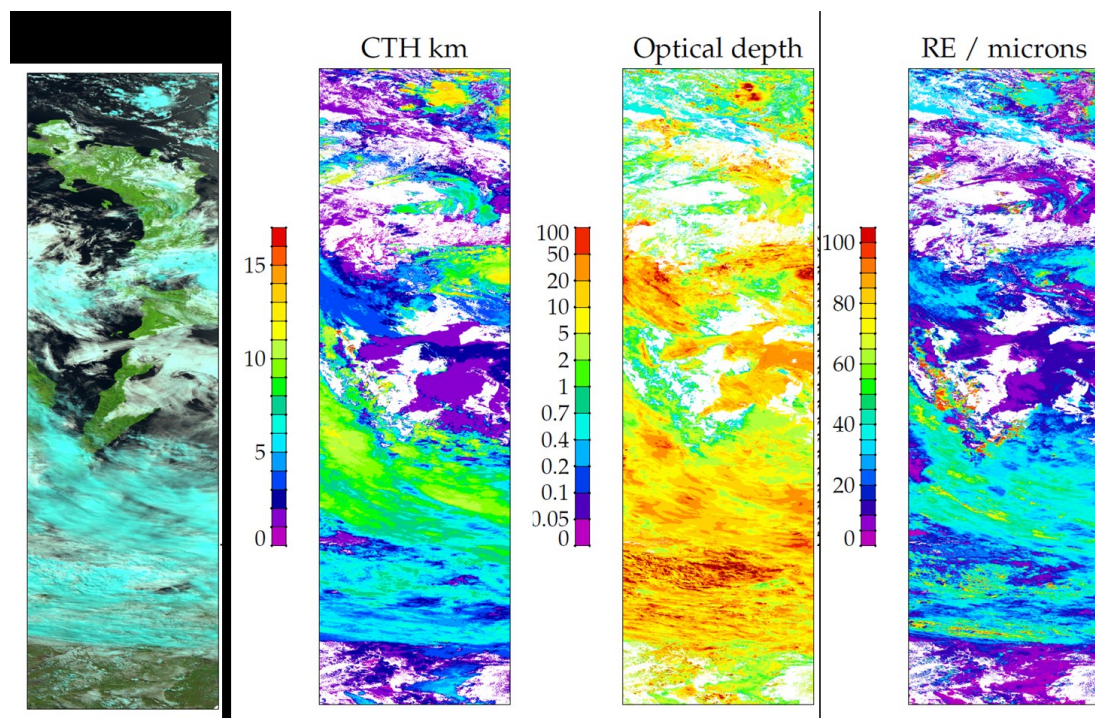


Figure 5: From left to right the images show a false colour image of the clouds as viewed by the visible channels on the AATSR satellite, the cloud top height (CTH) optical depth (i.e. thickness of the cloud) and effective radius of the particles visible at the top of the cloud.

- [1] M. Stengel et al. The Clouds Climate Change Initiative: The assessment of state of the art cloud property retrieval schemes applied to AVHRR heritage measurements, accepted Remote Sensing of the environment 2013
- [2] Poulsen, C. A., Siddans, R., Thomas, G. E., Sayer, A. M., Grainger, R. G., Campmany, E., Dean, S. M., Arnold, C., & Watts, P. D. (2012). Cloud retrievals from satellite data using optimal estimation: evaluation and application to ATSR, Atmospheric Measurement Techniques, 5, 1889-1910

3.2 R. J. Dance, N. C. Woolsey, (York Plasma Institute, Department of Physics, University of York), A. P. L. Robinson, (STFC CLF)

3.2.1 Hybrid-PIC simulation of relativistic electron beams in solid density targets

Successful application of laser-driven relativistic electron beams to diverse research fields such as fusion energy [1] and the generation of secondary sources of particles or x-rays [2,3] depends upon detailed understanding of how an electron beam travels through dense materials. The rather simple concept of the electron beam divergence, dominates the topic of electron beam transport. Through using the SCARF-LEXICON cluster with the hybrid-PIC model Zephyros [4], and a set of unique experimental measurements from the Central Laser Facility’s Vulcan petawatt laser, we aim to understand how relativistic electron beams move through solids, and how the divergence is affected by laser parameters and material properties such as density and resistivity.

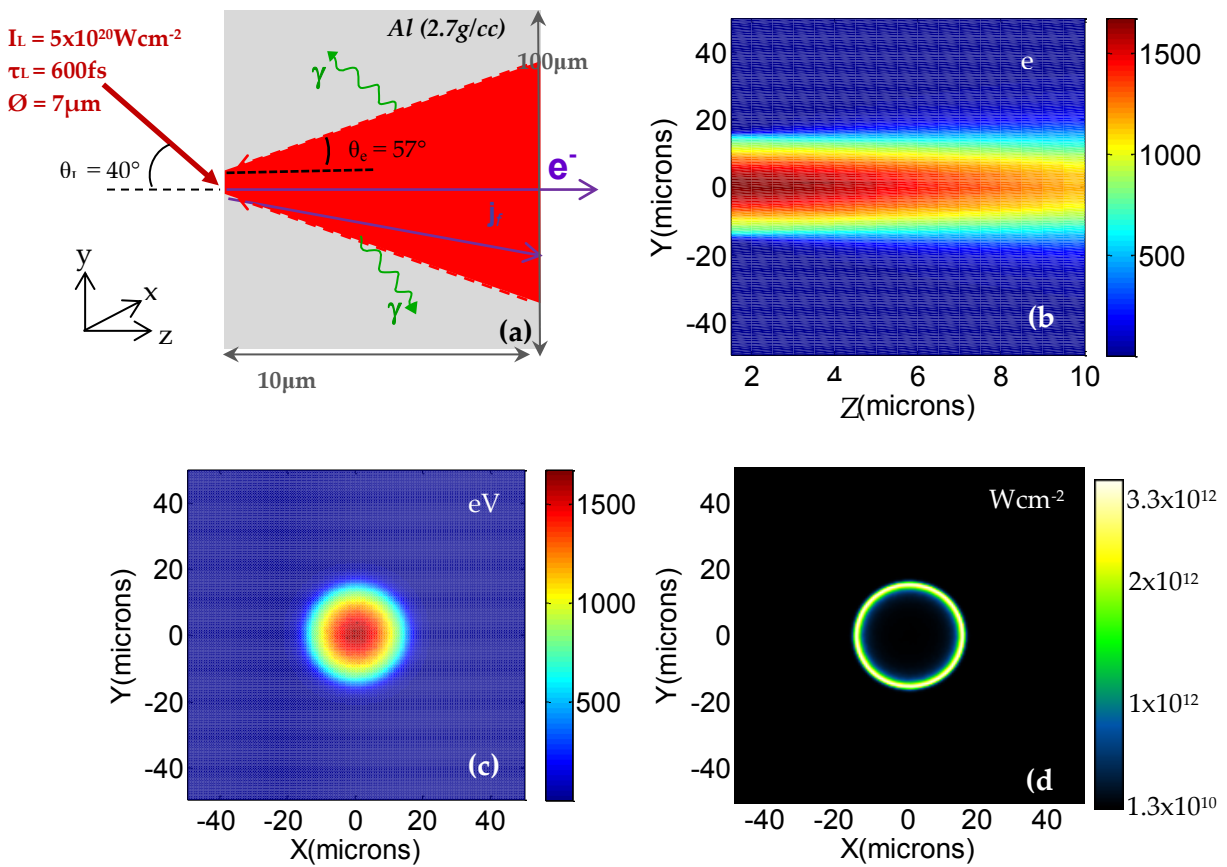


Figure 6: (a) - Zephyros simulation arrangement – ultra-intense laser pulse of intensity I_L and duration τ_L incident at the front surface of a thin, solid density aluminium foil at an angle of θ_L . Resistivity (presist) is calculated by the Lee - More resistivity model, and the fast electron injection angle (θ_e) is a free parameter (b) resulting background temperature viewed from the side of the target, with the laser propagating in the Z direction. (c) Temperature profile as in (b) but viewed at $Z = 5 \mu\text{m}$ alongside a post-processed image (d) showing the corresponding emission of 1.8keV x-rays. All images are taken at $t = 600 \text{ fs}$.

The Vulcan petawatt is capable of focussing around 150 J in 700fs into a 7 μm diameter focal spot producing a laser intensities of the order of $5 \times 10^{20} \text{ W cm}^{-2}$. With a laser wavelength of 1.053 μm this leads to a normalised $a_0 \approx 20$ and a relativistic electron beam. The hot electron temperature scaling with a_0 is relatively well known [5], giving a temperature of 6 MeV and a current density of $10^{23} \text{ A cm}^{-2}$. The experimental conditions are too extreme to take direct measurements of the physical processes taking place inside the target so the emission of x-rays, electrons or ions is utilised to infer

plasma conditions. For more in-depth interpretation (and also predictive modelling) Zephyros calculations can be used. In these calculations the plasma is treated as an amalgam of charged particles and plasma fluid elements, and outputs which include the plasma temperature and density are further processed to enable comparison with measurement.

For interpreting experiment, further processing is needed to render Zephyros calculations (of plasma temperature and density for example) in to time and space resolved x-ray emissivity. This requires the use of atomic physics and spectral synthesis models [6] to generate synthetic data which can be compared to experimental measurement. The intensity of the x-ray emission is strongly dependent on the temperature within the target, and as such x-ray measurements can be used as a temperature diagnostic, which constrain the Zephyros calculations.

Using the Zephyros model to generate synthetic data we are able to more accurately interpret our measurements and show, for example, the spatial distribution of temperatures in a target are sufficient to explain observed annular structures in the x-ray emission. Furthermore, these measurements provide spatially resolved temperatures providing a robust test of electron transport plasma models such as Zephyros. This work continues in support of an anticipated publication (in preparation for 2013), and data simulated here was also presented at several conferences talks in the UK and internationally including the 12th International Workshop on Fast Ignition of Fusion Targets held in Napa Valley (2012), the Institute of Physics Plasma Physics Group Annual Conference at St Hughs College (2012), Oxford and the High Power Laser User Community Christmas Meeting (2011 and 2012).

The author would like to thank the Fusion Doctoral Training Network (DTN) and the UK Engineering and Physical Sciences Research Council (EPSRC) for their continuing support, and to the staff of the CLF for their valuable and ongoing assistance with this research.

- [1] J. S. Green, V. M. Ovchinnikov, R. G. Evans et al. Phys. Rev. Lett. **100**, 015003 (2008), M. N. Quinn, X H Yuan, X. X. Lin, D. C. Carroll, O. Tresca, R. J. Gray, M. Coury, C. Li, Y. T. Li, C. M. Brenner, A. P. L. Robinson, D. Neely, B. Zielbauer, B. Aurand, J. Fils, T. Kuehl, P. McKenna et al., PPCF **53**, 025007 (2011)
- [2] Max Tabak, James Hammer, Michael E. Glinsky, William L. Kruer, Scott C. Wilks, John Woodworth. E. Michael Campbell, Michael D. Perry et al., Phys. Plasmas **1**, 1626 (1994)
- [3] M. Tabak, D. S. Clark, S. P. Hatchett, M. H. Key, B. F. Lasinski et al., Phys. Plasmas **12** 057305 (2005)
- [4] A. P. L. Robinson et al., PRL **108**, 125004 (2012)
- [5] S. C. Wilks, W. Kruer, M. Tabak, A. Langdon, Phys. Rev. Lett. **69** 1383 (1992)
- [6] J. J. MacFarlane, I. E. Golovkin, P. Wang, P. R. Woodruff, and N. A. Pereyra, High Energy Density Phys., **3**, 181 (2007)

3.3 A. Miceli, R. Senesi (University of Rome Tor Vergata), G. Gorini (University of Milan Bicocca), C. Andreani (University of Rome Tor Vergata)

3.3.1 Improving multiple prompt gamma ray analysis technique

Prompt gamma ray analysis (PGAA) is a non-destructive technique based on the measurement of gamma-rays following neutron capture. The pattern of gamma-rays uniquely identifies the isotopes in the sample. The PGAA method is commonly used in materials science, chemistry, geology, mining, archaeology, environment, food analysis, and medicine. Below is a summary of simulations carried out on the SCARF cluster aimed at the improvement of the PGAA technique.

3.3.2 Localization of inclusions in multiple PGGA

A current limitation of the PGAA technique is gamma-ray self-absorption, i.e. attenuation of gamma-rays within the sample itself that may lead to significant errors in quantification and identification of isotopes. We plan to exploit the gamma-ray self-absorption and investigate the feasibility of using low energies gamma-rays (< 650 keV) to localize metal slabs inside extended objects. Gamma-rays generated from neutron capture inside the inclusion will be attenuated according to their position inside the sample. Using two back-to-back detectors on opposite sides of the sample one can measure the ratio of the gamma-ray intensities and calculate the approximate position of the slab. Information on position of the inclusion could be used to correct for the self-absorption and obtain more precise quantitative analysis. We simulated two back-to-back gamma ray detectors, two lead grids, and a 2x2x2 cm³ Fe sample with a 0.1 cm thick Cu slab using the Geant4 Monte Carlo code (Figure 7). The simulation was carried out for a water moderator at 293K at spallation source (MCNPX spectrum from S. Ansell, ISIS), representing the ISIS neutron spectrum. Figure 8 shows the ratio of intensities of Cu lines as a function of gamma ray energies for Cu slabs in a Fe matrix placed at -0.2 cm and 0.2 cm offset along the x axis. The peak ratio is well separated for the two offsets for all the gamma ray lines. Reconstructed positions of Cu slabs at different offsets were found to be within 0.1 cm from the actual positions.

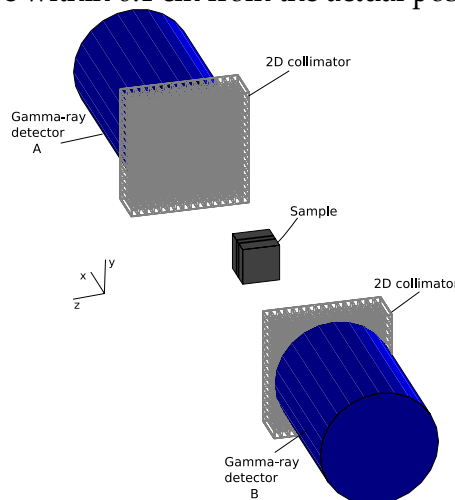


Figure 7: Simulated geometry. Gamma-ray detectors, 2D lead collimators, and sample are illustrated. The neutron beam, water moderator at 293K at a spallation source, was along the z axis [1].

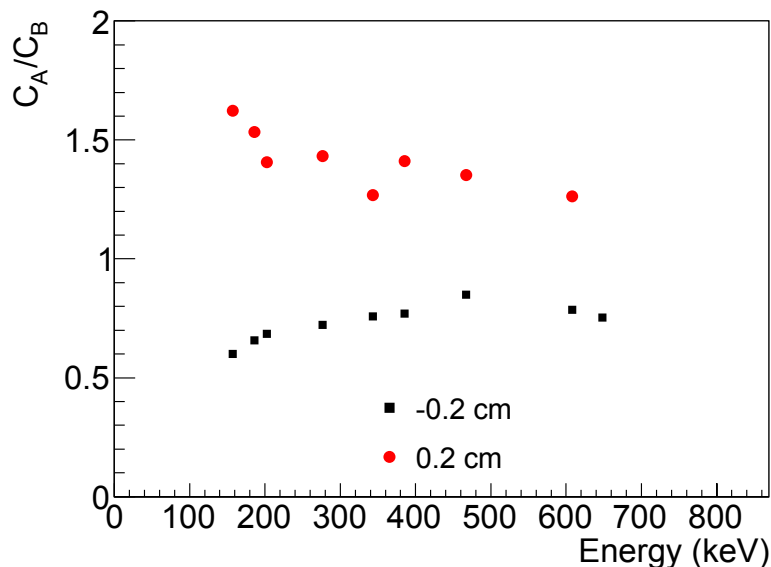


Figure 8: Ratio of counts on detector A and detector B as a function of gamma ray energies for a Cu slab in a Fe matrix placed at -0.2 cm (black) and 0.2 cm (red) offset along x [1].

3.3.3 PGGA with neutron time of flight

The background of the gamma ray spectrum generated by the blockhouse and the multitude of gamma-ray lines from the sample itself may result in peak overlapping and misidentification. Gamma ray lines of less abundant or weaker gamma-emitter isotopes could be discerned by selecting gamma-ray spectra at specific neutron time of flight (TOF) windows. Geant4 Monte Carlo simulations were employed to investigate the feasibility of the technique. Figure 9 shows a simulated PGGA spectrum integrated over all the neutron energies (up to 1200 eV) and in the neutron Cu resonances only (200 eV – 900 eV). The Cu peaks hardly visible in the spectrum integrated over all the neutron energies are clearly discernable in the PGGA spectrum centered at the Cu resonance.

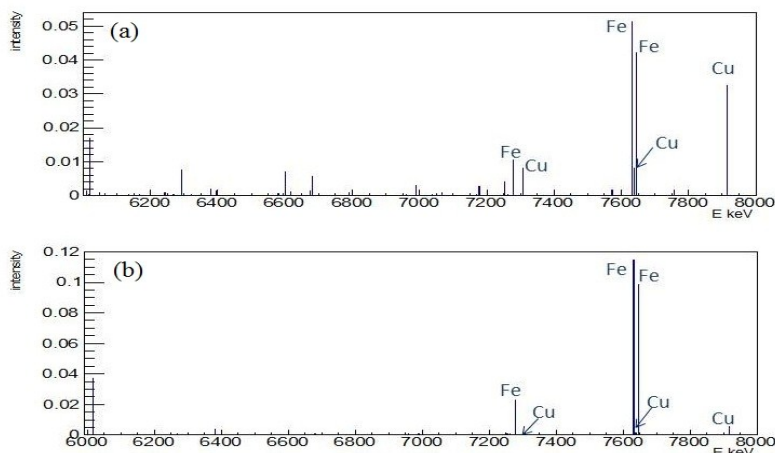


Figure 9: Simulated PGGA spectra integrated over (a) 200 ÷ 900 eV and (b) 0.025 eV ÷ 1200 eV neutron energies.

[1] Localization of inclusions in multiple prompt gamma ray analysis: a feasibility study A. Miceli et al. Journal of Physics: Conference Series (accepted)

3.4 V. Losasso (STFC Scientific Computing)

3.4.1 Computational studies of EGFR extracellular and intracellular domains

Epidermal growth factor receptor (EGFR) is the founding member of the ErbB family of receptor tyrosine kinases. These receptors regulate many physiological processes and are involved in the modulation of cell proliferation, differentiation, cell motility and apoptosis, thus being able to induce important mechanisms related to cancerogenesis [1]. Mutations affecting EGFR expression or activity and misregulation of EGFR signalling pathways have been implicated in several cancer types [2].

The EGFR protein can be divided into three domains: a ligand binding extracellular (EC) domain, a transmembrane (TM) domain and an intracellular (IC) domain. The IC domain contains a juxtamembrane (JM) segment, a kinase domain (KD) and a long regulatory C-terminal tail [3]. Ligand binding to the extracellular domain induces a conformational change which leads the intracellular kinase to form active asymmetric dimers [4].

Models of individual EGFR components, as well as of near-complete EGFR models (monomer, inactive dimer, active dimer) have recently been reported [5].

Our calculations on the SCARF cluster are focused on the description of both the EC and IC EGFR domains. In particular, we are simulating the EC domain in three different conformations: inactive monomer (Figure 10a), inactive dimer (Figure 10b) and active dimer (Figure 10c). These systems include also the TM region and the membrane. On the IC side, we are focusing on dimers of the kinase domain. They are simulated in the two possible conformations: symmetric (Figure 11a) and asymmetric (Figure 11b), and in complex with different ligands.

All these studies are carried out in close collaboration with the group of Marisa Martin-Fernandez at RAL. Indeed, we have already investigated several aspects of EGFR conformational changes by combining simulations and FRET microscopy [6-8]. With these new computational studies, we aim at providing a broader picture of the EGFR structural features, based on new FRET experimental data.

These studies would not be possible without the use of the SCARF cluster. Indeed, its many cores allow us to run simulations of the kinase domains in different conditions (starting conformation, ionic strength, bound ligands), as well as to investigate biologically relevant timescales of the bigger EC domain (up to ~400k atoms for the active dimer).

- | |
|---|
| <p>[1] Lemmon, M.A., and Schlessinger, J. (2010). Cell signaling by receptor tyrosine kinases. <i>Cell</i> 141, 1117-1134.</p> <p>[2] Riese, D.J., 2nd, Gallo, R.M., and Settleman, J. (2007). Mutational activation of ErbB family receptor tyrosine kinases: insights into mechanisms of signal transduction and tumorigenesis. <i>Bioessays</i> 29, 558-565.</p> <p>[3] Voldborg, B.R., Damstrup, L., Spang-Thomsen, M. and Poulsen, H.S. (1997). Epidermal growth factor receptor (EGFR) and EGFR mutations, function and possible role in clinical trials. <i>Ann Oncol</i> 8, 1197- 1206.</p> <p>[4] Zhang, X., Gureasko, J., Shen, K., Cole, P.A., and Kuriyan, J. (2006). An allosteric mechanism for activation of the kinase domain of epidermal growth factor receptor. <i>Cell</i> 125, 1137-1149.</p> <p>[5] Arkhipov, A., Shan, Y., Das, R., Endres, N.F., Eastwood, M.P., Wemmer, D.E., Kuriyan, J., and Shaw, D.E. (2013). <i>Cell</i> 152(3), 557-569.</p> <p>[6] Roberts S.K., Tynan C.J., Winn M.D., and Martin-Fernandez, M.L. (2012). Investigating extracellular in situ EGFR structure and conformational changes using FRET microscopy. <i>Biochem. Soc. Trans.</i> 40, 189-194.</p> <p>[7] Tynan C.J., Roberts S.K., Rolfe D.J., Clarke D.T., Loeffler H.H., Kästner J., Winn M.D., Parker P.J., and Martin-Fernandez M.L. (2011). Human-EGFR aligned on the plasma membrane adopts key features of Drosophila-EGFR asymmetry. <i>Mol.Cell.Biol.</i> 31, 2241-2252.</p> <p>[8] Kästner, J., Loeffler, H.H., Roberts, S.K., Martin-Fernandez, M.L., and Winn, M.D. (2009). Ectodomain orientation, conformational plasticity and oligomerization of ErbB1 extracellular domain. <i>J. Struct. Biol.</i></p> |
|---|

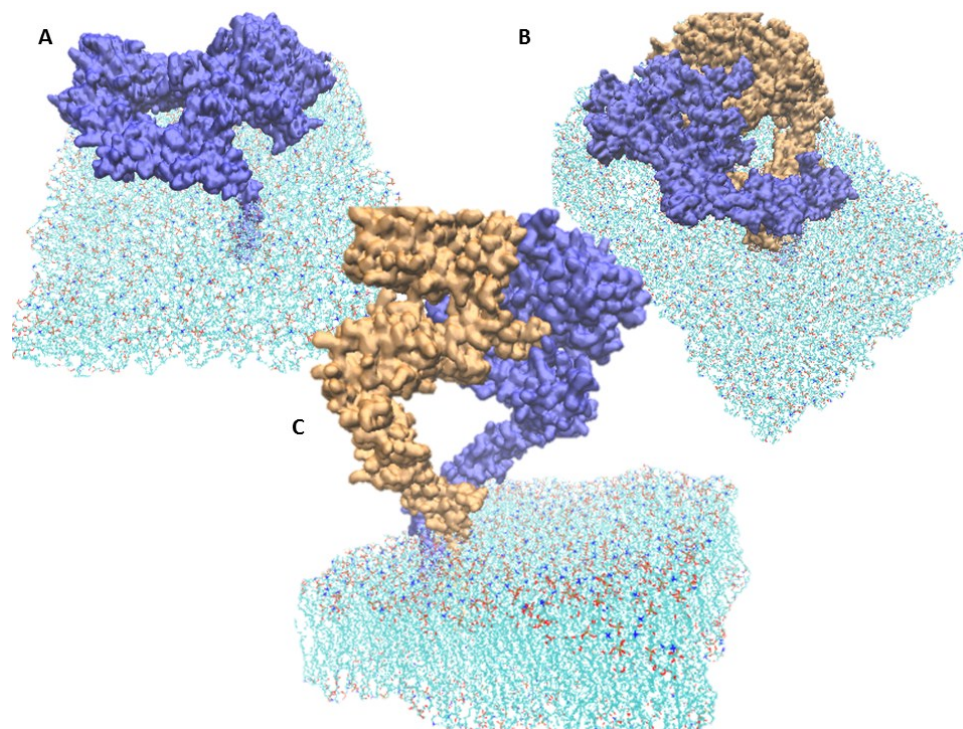


Figure 10: EGFR EC domain on membrane. A) inactive monomer; B) inactive dimer; C) active dimer. In B) and C), the two monomers are represented in different colours.

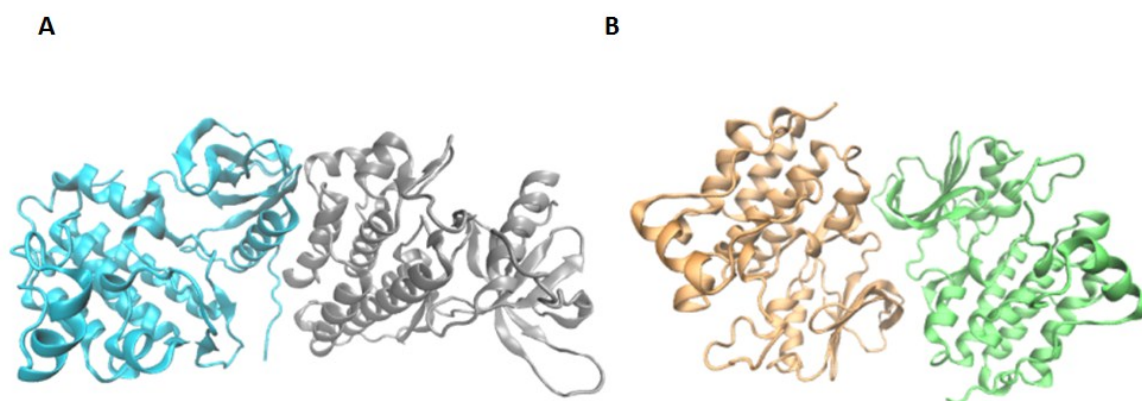


Figure 11: EGFR IC domain. A) asymmetric dimer; B) symmetric dimer. The two monomers are represented in different colours.

3.5 B. Pine, H. Smith, R. Williamson (ISIS)

3.5.1 Code Development for the ISIS Synchrotron Group

As well as using externally written codes to simulate the behaviour of the ISIS synchrotron, there is also a dedicated effort to produce software tools within the group. The advantages of this are two-fold: firstly a greater understanding of the simulation program and an ability to modify that program; secondly a strong emphasis on skills in the group which can support such a project, particularly programming and parallelisation techniques.

Our approach has been to split the transverse dynamics from the longitudinal and injection. Rob Williamson has been responsible for longitudinal motion, Hayley Smith for injection and Ben Pine for transverse motion. The various core components are now being merged into what is termed a “2.5D” simulation code, where transverse dynamics along the bunch of protons takes place in a series of discreet longitudinal slices. This strategy enables a reasonably straight-forward parallelisation approach in which each transverse slice exists on a separate processor and longitudinal motion can move particles between the processors. As longitudinal motion is slow relative to transverse this approach should be justified.

The combined code is now being benchmarked against ORBIT simulations produced by Dean Adams which model part of the ISIS cycle. Once these have been completed the goal will be to explore specific features of ISIS such as the strong image fields from off-centre beams. The simulation code will also be used to study ISIS upgrades. One option is to increase the energy of the linac from 70 MeV to 180 MeV. This would lower the forces acting between particles in the high intensity beam, and along with matching the injected beam better to the ring allow for a greater intensity to be accelerated. This fairly cost-effective upgrade could more than double the beam power available to the targets.

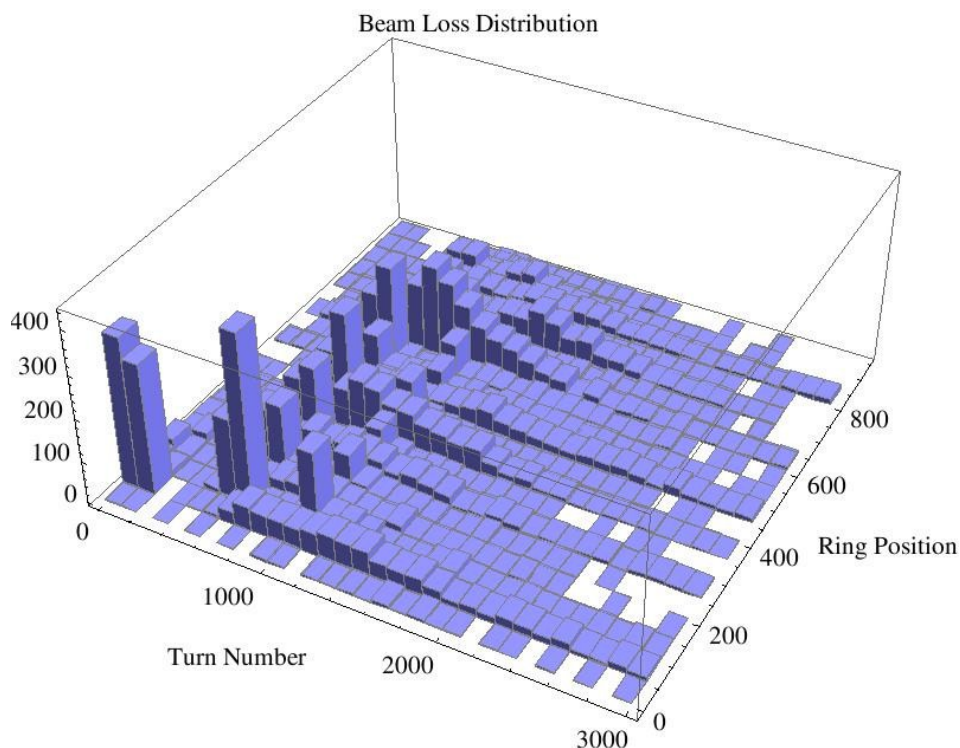


Figure 12: Beam loss as a function of ring position and turn number.

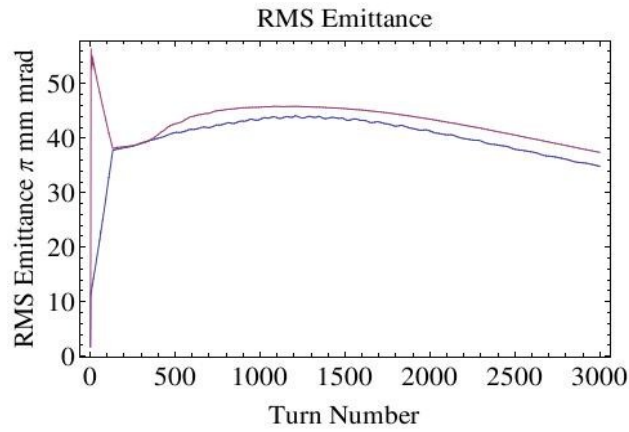


Figure 13: RMS beam emittances (blue H, red V) plotted against turn number

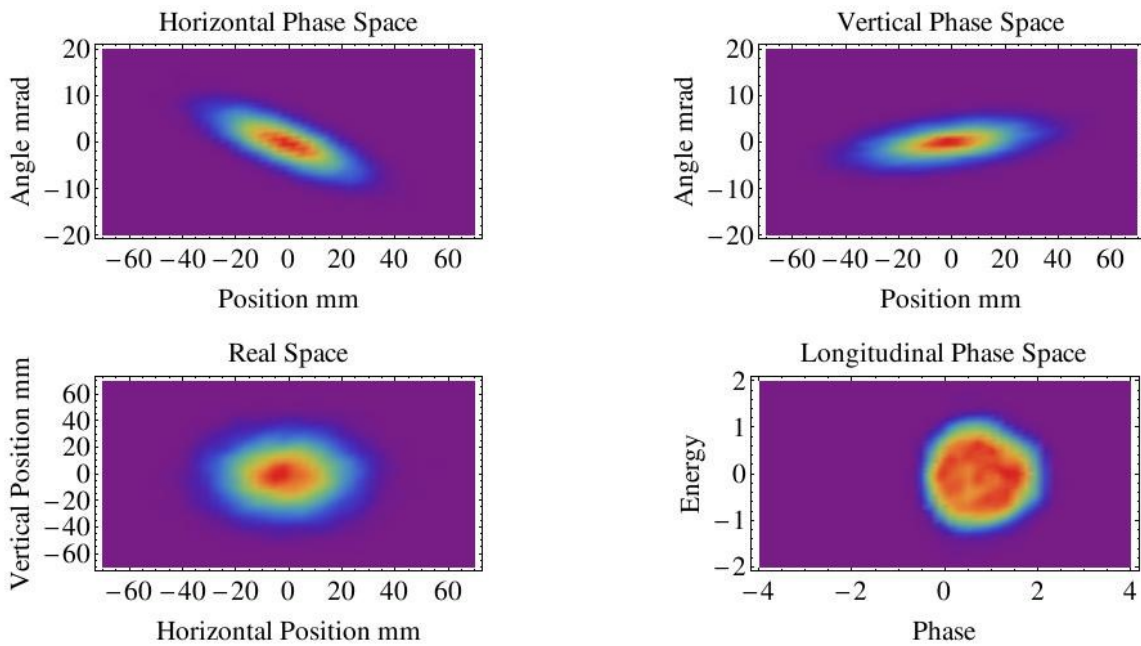


Figure 14: Horizontal, vertical and longitudinal phase space along with real space at turn 2676

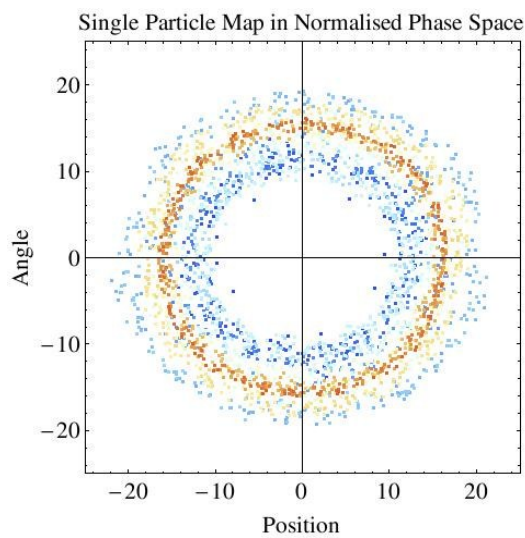


Figure 15: Poincare map of a single particle over 3000 turns in normalised phase space, where the colour from blue to red represents start to end of the simulation.

3.6 H. Loeffler (STFC Scientific Computing)

3.6.1 Free energy simulations of protein-ligand complexes and automatic setup tool development

The free energy of binding of a ligand to a protein is a key quantity in biochemistry. It is an indicator of how strong the ligand will bind. This is especially valuable in drug development where potentially thousands of small molecule ligands can be rapidly screened for its potency *in silico*.

I currently work on the EGFR (epidermal growth factor receptor) family of receptors. Malfunctioning in this family is implicated in various forms of cancer and other medical conditions. Several small ligand drugs have been developed to treat these diseases. A deeper understanding of the underlying molecular processes involved is essential in progressing the field. A valuable tool to tackle this problem computationally is applying the Molecular Dynamics (MD) technique. MD algorithms have been parallelized and can therefore benefit tremendously from current parallel computing platforms.

In conjunction with the scientific case, I develop an automatic setup tool, currently called SimSetup, for free energy calculations which can quickly derive necessary simulation parameters for large amounts of ligands and ease the tedious setup process for the human operator. Preliminary work on free energies has been published in DOI:10.1002/prot.24339. SimSetup has been introduced at the annual CCP-BioSim conference 2013 in Nottingham.

SCARF is an excellent platform to carry out this type of computations because both simulations and analysis require literally thousands of individual and (partially) independent jobs to be carried out. MD is done moderately parallel utilizing 36 to 48 cores. The superb job throughput on SCARF has advanced this project to a great extent.

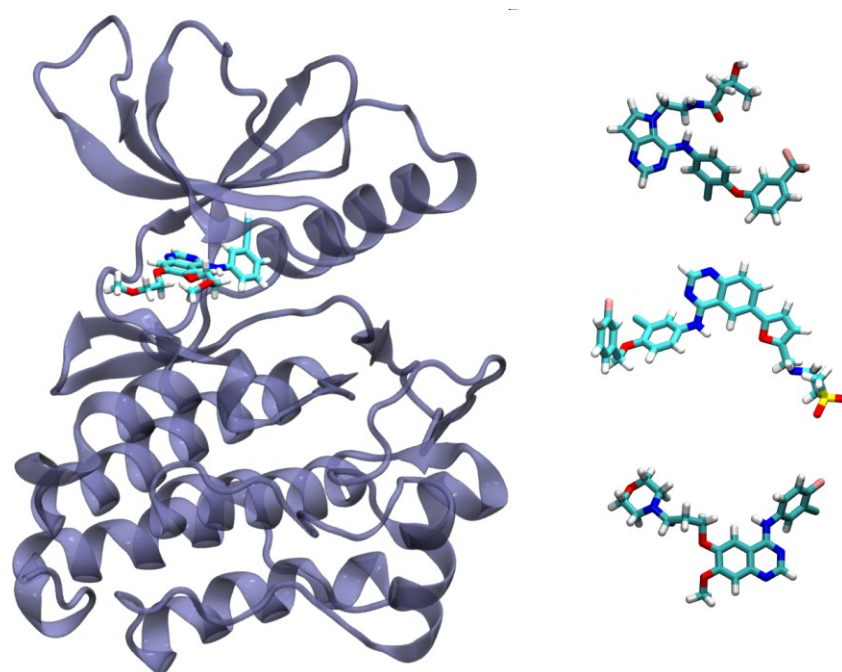


Figure 16: The EGFR kinase bound to a ligand.

Does any of the three ligands on the right bind stronger? Does the protein conformation matter? High throughput free energy simulations can help in answering such questions.

3.7 A.P.L.Robinson, R.M.G.M.Trines, R.H.H.Scott, and P.A.Norreys (STFC CLF)

3.7.1 Fast Electron Transport

Understanding the flow of extremely high-current laser-generated relativistic electron beams through dense plasmas is a crucial matter in ultra-intense laser-plasma physics. Most UHI (ultra-high intensity) laser-solid interactions produce fast electron beams which lead to a number of phenomena of interest to many researchers. Fast electron beams are also pivotal in an advanced variant of inertial fusion known as ‘Fast Ignition’ which in principle is a potential route to high energy gain (>100) perhaps even with sub-MJ total laser energies.

Dr.Robinson and Dr.Schmitz are studying fast electron transport guided by engineered resistivity gradients as part of a project funded by the European Research Council (ERC) called STRUCMAGFAST. This has involved carrying out studies with the 3D Zephyros code on the LEXICON II resource, as well developing Zephyro’s successor code. In recent publications, Dr.Robinson and Dr.Schmitz have shown [1] that a simple guiding concept based on a self-generated ellipsoidal magnetic mirror might improve coupling in the Fast Ignition scheme by 3-4 times, even if the angular divergence of the fast electrons is quite high. Dr. Robinson and Dr.Schmitz have also looked [2] at how to effectively confine fast electrons in a simple wire-in-substrate target. In this configuration the wire can be heated strongly, but without significant heating to the substrate. This can lead to the wire expansion driving strong hydrodynamic motion in the substrate which might be used for a number of interesting radiation-hydrodynamics and laboratory astrophysics experiments.

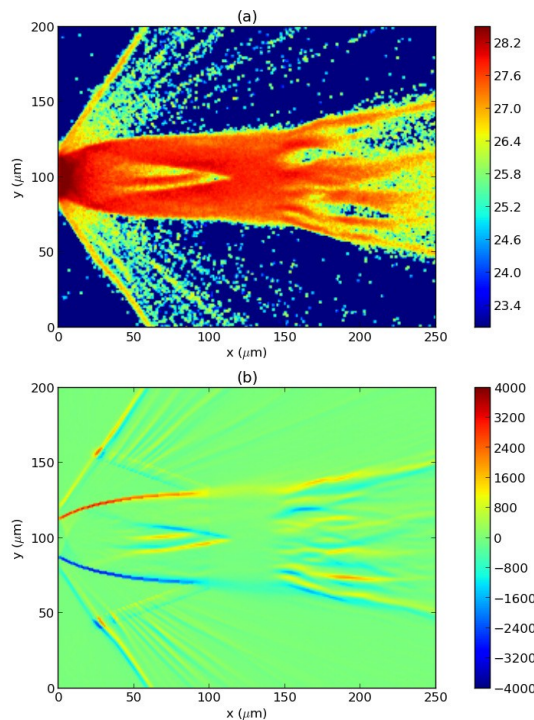


Figure 17: Top : Fast electron density in a simulation with a self-generated magnetic elliptical mirror formed by exploiting magnetic field growth at resistivity gradients.

Bottom : Magnetic flux density (z-component) in a simulation with a self-generated magnetic elliptical mirror. The strong elliptical mirror fields can be seen between 0 and 100 microns.

3.7.2 *Fast Electron Generation*

The generation of fast electrons in ultra-intense laser-plasma interactions is critical to many different areas of laser-plasma physics and interests. These include multi-MeV proton and ion acceleration, x-ray generation, and positron production amongst others.

The mechanisms that lead to the generation of the very highest energy electrons in laser-solid interactions are still a matter of considerable uncertainty. In one body of work that Dr. Robinson and his collaborator Dr. Alex Arefiev (University of Texas) have been involved in over the past year this has been investigated [3]. It was found that there is an over-looked mechanism by which “super-ponderomotive” electrons (those which reach energies in excess of $\frac{1}{2}a_0^2 m_e c^2$). In this mechanism, the electrons receive a well-timed boost by a self-generated electrostatic field in the direction of the incident laser pulse. This does not significantly accelerate the electron, but it does lead to a significant reduction of the rate at which the electron dephases from the laser field. This leads to much greater acceleration by the incident laser field, even achieving super-ponderomotive energies. Dr. Robinson used the SCARF-LEXICON II resource to carry out parametric arrays of PIC simulations as part of this study [3].

One of the principal barriers to the viability of the Fast Ignition Inertial Fusion scheme is the high divergence of the fast electron beam. Dr Scott has been performing computationally intensive particle-in-cell numerical modelling on Scarf Lexicon II. This has the aim of modifying the geometry of the laser-plasma interaction in such a way that the fast electron beam generated by the interaction would be convergent. If realised this may be beneficial for the Fast Ignition Inertial Fusion scheme as it should reduce the laser energy required, making the scheme more viable. This work is ongoing.

3.7.3 *Brillouin amplification*

Brillouin amplification, like Raman amplification is a process by which two laser beams couple in plasma via a plasma beat wave. The goal of this process is to transfer the energy from a long laser pulse at low intensity to a much shorter laser pulse at high intensity, thus creating a plasma-based laser pulse compressor. Brillouin amplification differs from Raman amplification in that the laser pulses couple via an ion-acoustic plasma wave, while they couple via a Langmuir (electron) wave in Raman amplification. As a result, Brillouin amplification has a lower growth rate and compression ratio than Raman scattering, but it is also more tolerant regarding fluctuations in the plasma temperature and density. It is therefore a viable alternative to Raman amplification, especially for the compression of long pulses at moderate intensity but high total energy.

K. Humphrey and R. Trines have investigated Brillouin amplification via numerical simulations on Scarf-Lexicon, using the particle-in-cell code Osiris. They have identified the laser and plasma conditions for which Brillouin amplification is efficient and does not suffer from parasitic instabilities that degrade the quality of the final compressed pulse. They have also shown that the duration of the compressed pulse can be controlled via the intensity of the pump beam, opening up the possibility of tailored laser pulses [6]. Furthermore, they have shown that collisional effects can strongly reduce the level of spontaneous, premature Brillouin scattering of the pump pulse, thus improving the contrast of the compressed pulse. This latter result has been accepted for publication and is now in press [7].

3.7.4 High-harmonic generation in oblique laser-plasma interactions

In laser-target interaction, especially when long (nanosecond) or strongly focused pulses are used, the laser impact will generate a halo of ablated plasma, extending from the impact spot. This plasma halo can have a scale length of many microns, and extend over a fairly long distance from the target. Its presence will strongly modify any subsequent laser-target interactions. This is especially important in the case of high-harmonic generation (HHG) in oblique laser-solid interactions. Most of the models for laser reflection and HHG assume that the target surface is a “hard-edged” moving mirror. Also, most theoretical studies of HHG are one-dimensional and do not cover the angular distribution of the emitted harmonics. However, a preplasma with a 3-5 μm scale length is anything like “hard-edged” to a laser pulse with 1 μm wave length. Similarly, the reflection of a laser beam by a target in the presence of a preplasma can be very different from the usual “specular reflection”. Thus, the angular distribution of the emitted harmonics deserves close scrutiny as well.

W. Boeke-West and R. Trines have studied the reflection and high-harmonic generation by a laser pulse that obliquely hits a solid target preceded by a preplasma. This has been done via 2-dimensional particle-in-cell simulations using the code Osiris, so the harmonics spectrum could be studied over a range of angles simultaneously. It has been found that the presence of a preplasma causes laser light to be scattered in many directions (“beam spray”). Most tellingly, surface waves, that propagate almost perpendicularly to the target-normal direction, cause side-scattering of laser light in the same direction, i.e. almost parallel to the target surface, and towards the incoming laser beam.

It was found that increasing the density gradient scale length would cause the harmonics of the laser frequency to broaden and become less clearly defined. Increasing the laser intensity would lead to strong plasma turbulence, and the presence of surface waves on the target surface. In turn, this would lead to strong (harmonic) radiation emission in a direction (almost) parallel to the target surface, and ejection of plasma electrons in the same direction. The results have been reported in Ref. [8].

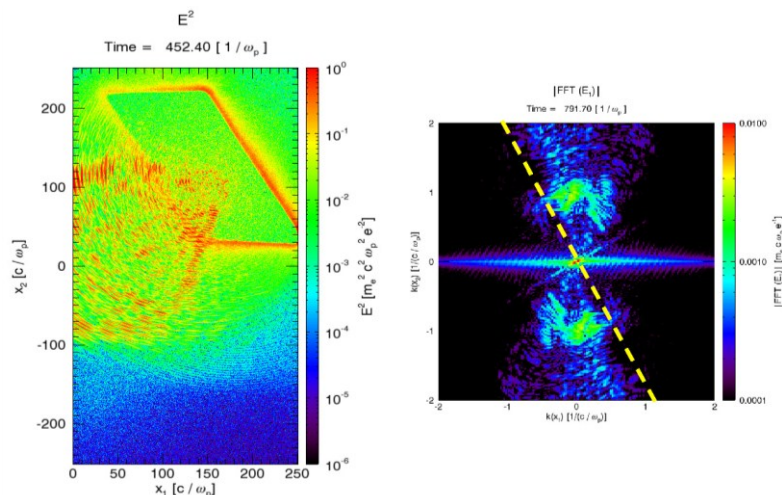


Figure 18: Left: Laser intensity distribution for the interaction of an intense (1019 Wcm⁻²) short (125 fs) laser pulse with a solid target having a long scale length (4 micron). Right: Fourier spectrum of the longitudinal component of the laser electric field.

From these plots, it is clear that most of the laser's energy is not scattered in the "specular" direction, and that harmonics of the highest intensity can be observed at an angle close to the target surface (yellow dashed line).

3.7.5 CLF User Support

A large part of the PPG's work is providing support to the CLF's User community to ensure that computational and theoretical support is available to maximize the impact of the research carried out on the CLF's laser systems.

Dr. Robinson has continued to develop and provide the Zephyros hybrid code for CLF Users. This has included tailoring Zephyros to meet specific user requirements, as well as helping users to make use of the code and understand the results from it. The Zephyros User Community includes:

- University of York : R.Dance, D.Blackman
- Oxford University : T.White
- Queen's University Belfast : M.Makita
- Strathclyde University : D.Maclellan, M.Coury

Recent publications from this group of users which have combined experimental studies with Zephyros simulations include [4] and [5].

During the summer of 2012, a user experiment led by P. Norreys was carried out on the Vulcan laser to investigate the possibility of Brillouin amplification, as well as the competition between Raman and Brillouin scattering processes, on the Vulcan laser system at the CLF. Simulations in support of this experiment have been carried out by K. Humphrey and R. Trines. The simulation results showed good agreement with the experimentally obtained frequency spectra, and provided deeper insight in the competition between various processes that took place during the interaction between the laser pulses and the plasma. All results have been reported in Ref. [9].

In addition, R. Trines provides on-going support to students and senior researchers in the CLF user community that wish to make use of the CLF-owned Scarf-Lexicon cluster, which is maintained by the Scientific Computing department. This pertains in particular to: Jimmy Holloway (UCL), Nicolas Bourgeois (Oxford University), Mireille Coury (U. Strathclyde) and R. Dance (U. York).

It has been shown both theoretically and experimentally that multiple ultra-high intensity laser pulses can generate electron and ion beams with better properties than those generated from a single pulse. The physics of this interaction is however hard to study due to the extreme conditions of temperature, density and ultra-short pulse durations. Dr Scott has been performing radiation-hydrodynamics simulations with the FLASH code [10] on Scarf Lexicon II for users of the Central Laser Facility in order to model the hydrodynamic expansion which occurs between ultra-high laser pulses. This work has included developing a version of the FLASH code with modified laser-absorption characteristics. This work is ongoing.

- [1] A.P.L.Robinson and H.Schmitz, *Phys.Plasmas*, **20**, 062704 (2013)
- [2] A.P.L.Robinson and H.Schmitz, Submitted (2013)
- [3] A.P.L.Robinson, A.V.Arefiev, and D.Neely, *Phys.Rev.Lett.*, **111**, 065002 (2013)
- [4] M.Coury et al., *Phys.Plasmas* **20**, 043104 (2013)
- [5] D.Maclellan et al., *Phys.Rev.Lett.*, **111**, 095001 (2013)
- [6] K. Humphrey, P. Alves, R. Trines et al., "Production of petawatt laser pulses of picosecond duration via Brillouin amplification of nanosecond laser beams", in preparation (2013).
- [7] K. Humphrey, F. Fiuza, R. Trines et al., "Effect of collisions on amplification of laser beams by Brillouin scattering in plasmas", *Phys. Plasmas*, in press (2013).
- [8] W. Boekee-West, R. Trines, A. Machacek and P. Norreys, "Angular distribution of high harmonics generated during laser-preplasma interaction", in preparation (2013).
- [9] E. Guillaume et al., "Efficient laser pulse amplification by stimulated Brillouin scattering", in preparation (2013).
- [10] B. Fryxell *et al.* 2000 *ApJS* **131** 273

3.8 G. Graziano (University College London), F. Fernandez-Alonso (ISIS), A. Michaelides (University College London)

3.8.1 Towards a better understanding of the role of van der Waals interactions on adsorption: hydrogen on layered materials

The SCARF cluster has been used to study the hydrogen physisorption on different layered materials using density functional theory (DFT). The hydrogen physisorption process is highly dominated by long range, van der Waals (vdW) interactions. These interactions are fundamental for a large number of systems and natural processes, however the computational description is still difficult especially in the DFT frame. In the last decade different functionals have been developed in order to account properly for the long range interactions [1]. In this study we have used several vdW-functionals in order to understand the role of the vdW forces associated with the hydrogen adsorption on different substrates. The substrates investigated are: graphite, *hexagonal*-boron nitride (*h*-BN) and some transition metal dichalcogenides such as MoS₂, MoSe₂, MoTe₂, WS₂ TiSe₂. We performed our calculations using the plane-wave basis set code VASP 5.3 and five different exchange-correlation functionals: optimized Becke88 van der Waals (optB88-vdW) [2], optimized PBE van der Waals (optPBE-vdW) [2], vdW-DF2 [3], DFT-D [4] and the Tkatchenko-Scheffler PBE (TS-PBE) [5].

We first look at different hydrogen positions and orientations on each substrate. The calculations do not highlight any preferential configuration for the gas molecule. The hydrogen adsorption energy has also been calculated on the different surfaces. Although the adsorption energies on the different layered materials are very similar, ranging within 20 meV/H₂ from each other, it is still possible to highlight a precise trend among the values. All the functionals predict the higher hydrogen adsorption energies on graphite and *h*-BN; optB88-vdW for instance predicts adsorption energies of about 80 meV/H₂. In the case of the transition metal dichalcogenides the different transition metal, like for MoS₂, WS₂, and TiSe₂ does not affect the adsorption energy which is ~ -64 meV/H₂ as calculated with the optB88-vdW.

The different chalcogen atom, on the other hand ends up in a decrease of about 8 meV/H₂ moving from the sulphur to the tellurium. The same trend is always verified by all the functionals tested. The overall similarity of the adsorption energies can be explained as a fine interplay between the attractive and repulsive interactions. We decomposed the adsorption energies calculated with the optB88-vdW functional to its different contributions. The local and non-local energies account for the short and long range attraction. The remaining terms of the Kohn-Sham equation, including the exchange energy, account for the repulsive interactions. The figure below summarises this decomposition and clearly shows that the balance between repulsion and attraction results in the same adsorption energy for the hydrogen on different layered materials.

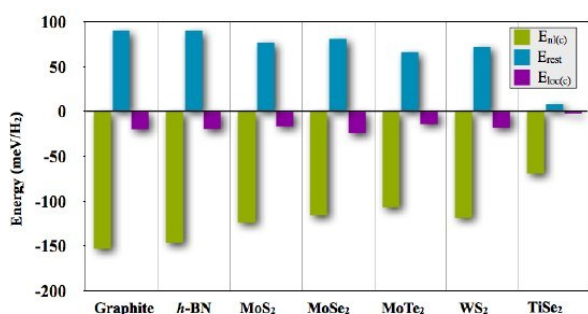


Figure 19: Decomposition of the adsorption energy of molecular hydrogen on the surface of the layered materials obtained with the optB88-vdW functional. The negative values are due to the correlation energy, specifically to the non-local (green bars) and local (purple bars). The positive values refer to the sum of the exchange and the remaining Kohn-Sham energy (blue

bars).

3.9 G. Graziano (University College London), M. J. Gutmann (ISIS), J. Klimeš (University of Vienna), A. Michaelides (University College London), F. Fernandez-Alonso (ISIS)

3.9.1 *Anisotropic Displacement Parameters and Diffuse Scattering in Soft Layered Materials: The Case of Graphite*

Layered materials, such as graphite, are characterized by a strong anisotropy in the binding forces. The bonds between atoms in each layer are strong and largely covalent, while binding between layers is much weaker, involving van der Waals (vdW) interactions. Despite the large technological impact due to the anisotropy, a full experimental description of such property and in general of the layered materials is not available. In addition some of the fundamental properties of layered materials (e.g. the interlayer binding energy) are not easily accessible experimentally. The development of new computational techniques, like new functionals within the density functional theory (DFT) frame able to capture both short- and long-range interactions, can be used to fill this gap. We have already tested that some functionals, e.g. optB88-vdW [1], perform better than others in predicting interlayer binding energies [2].

In this work we used one of the standard DFT functional that does not account for the vdW interactions, LDA, and the newly developed optB88-vdW to calculate the graphite phonon dispersion relations. Following the procedure developed by Gutmann et al. [3] it was possible to extract the diffuse scattering patterns and the anisotropic displacement parameters (ADPs) from the calculated phonon dispersion relation.

Indeed the anisotropy in the bonding results in different in-plane and out-of-plane dynamics, which can be probed experimentally with X-rays and neutrons. Diffuse-scattering data and ADPs as a function of temperature for graphite have been obtained using single-crystal neutron diffraction (SXND) on the SXD diffractometer at the ISIS Pulsed Neutron and Muon Source and on the BW5 high-energy X-ray diffractometer at the HASYLAB/DESY in Hamburg. The comparison of theoretical predictions using DFT functionals against experimental has established the sensitivity of SXND to vibrational motions along different crystallographic directions. This result proves that a diffractometer can also be used to gain some knowledge about the dynamics of the atom in the materials. Moreover, these experimental results provide benchmarks of the performance of newly developed DFT functional [1,2] that attempts to describe both local and non-local interactions in soft layered materials.

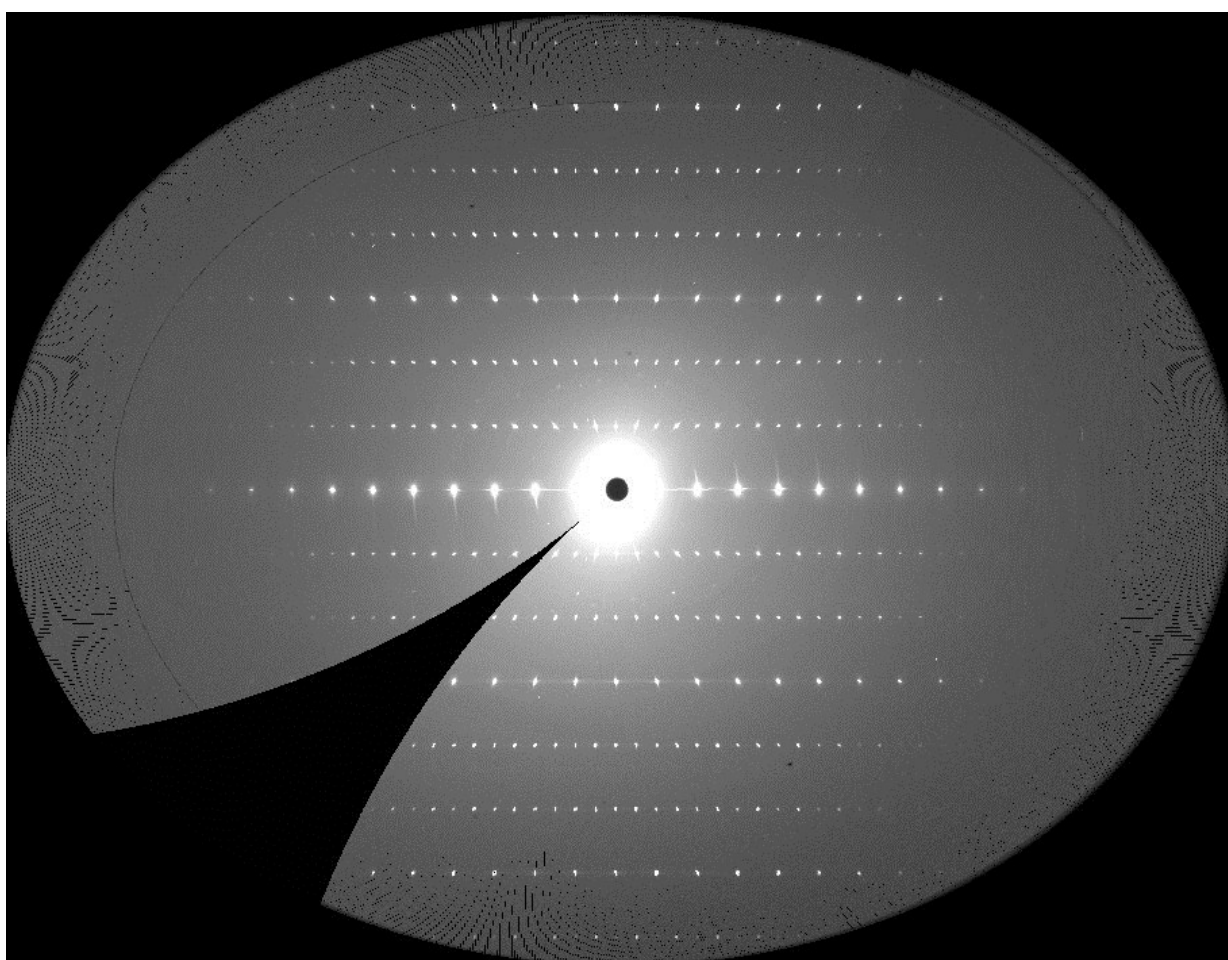
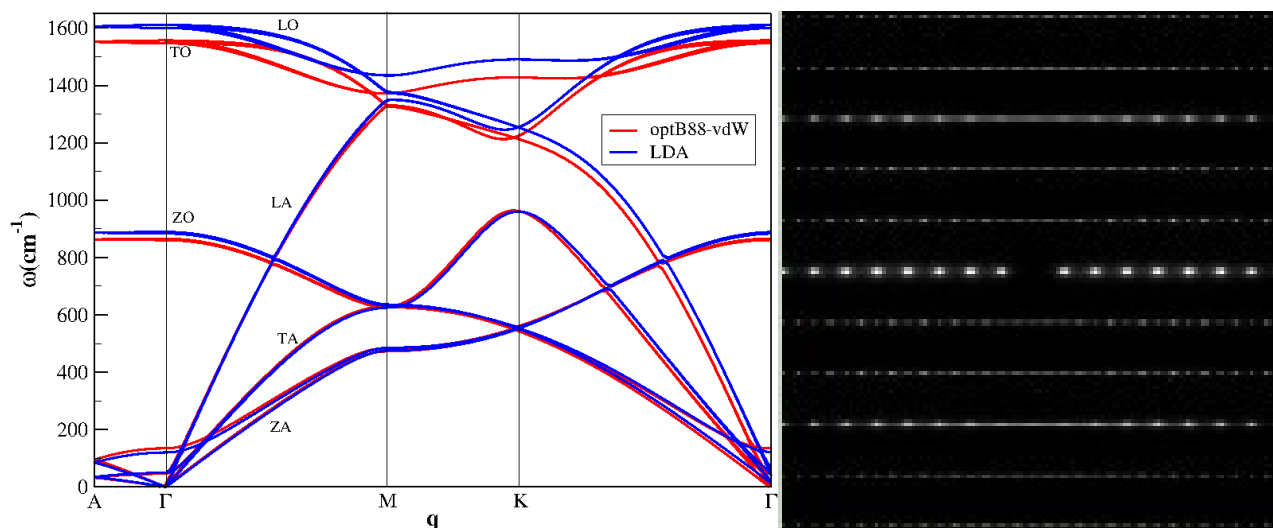


Figure 20: Previous Page Left: Phonon dispersion relations calculated using the optB88-vdW (red lines) and the LDA (blue lines) functionals at 0K. Previous Page Right: Simulated diffraction pattern for the $h0l$ plane. Above: X-ray diffraction for the $h0l$ patterns obtained with high-energy diffractometer. The experimental diffraction pattern has been obtained using the high-energy X-ray diffractometer at the HASYLAB/DESY in Hamburg.

Lattice Constants (Å)							
	Calculations (0K)		SXND				
	LDA	optB88-vdW	5K	50K	100K	200K	300K
a=b	2.4462	2.4600	2.4610±0.0012	2.4613±0.0019	2.4616±0.0019	2.4624±0.0019	2.4615±0.0019
c	6.5997	6.6000	6.6719±0.0034	6.6768±0.0097	6.6808±0.0102	6.6958±0.0101	6.7117±0.0102
ADPs (Å ²)							
U₁₁=U₂₂	0.001658	0.001687	0.001719±0.000129	0.001659±0.000146	0.001873±0.000133	0.001946±0.000161	0.002113±0.000171
U₃₃	0.003162	0.003149	0.003827±0.000192	0.004394±0.000221	0.005212±0.000204	0.007717±0.000291	0.011022±0.000370
U_{iso}	0.002160	0.002175	0.002422±0.000086	0.002571±0.000098	0.002986±0.000090	0.003869±0.000121	0.005083±0.00145

Figure 21: The table in green shows the graphite in-plane (a and b) and out-of-plane (c) lattice constants calculated at 0K using the LDA and the optB88-vdW functionals. In the five last columns the experimental lattice constants as a function of the T are reported. The orange table reports the comparison between the calculated and experimental anisotropic displacement parameters (ADPs). U₁₁ and U₂₂ refers to the in-plane ADPs, U₃₃ to the out-of-plane ADP, and U_{iso} refers to the total, isotropic displacement. All the experimental data have been collected using the SXD diffractometer at the ISIS Pulsed Neutron and Muon Source.

This work has been presented as poster at the International conference on Neutron Scattering. (Edinburgh 8-12 July 2013).

This work complements the following experiments conducted at ISIS Pulsed Neutron and Muon Source:

- Thermal Expansion and Diffuse Scattering of Graphite and Hexagonal-Boron Nitride. (*SXD Diffractometer*)
- Benchmarking New van-der-Waals Functionals for Soft Layered Materials. (*TOSCA Spectrometer*)
- Accurate comparison of the anisotropies of graphite and hexagonal boron nitride by deep inelastic neutron scattering. (*VESUVIO Spectrometer*)

- [1] J. Klimeš, D. R. Bowler and A. Michaelides, *J. Phys.: Condens. Matter* 22, 022201 (2010).
- [2] G. Graziano, J. Klimeš, F. Fernandez-Alonso, A. Michaelides, *J. Phys.: Condens. Matter* 24, 424216 (2012).
- [3] M. J. Gutmann, K. Refson, M. v. Zimmermann, I. P. Swainson A. Dabkowski, and H. Dabkowska, *J. Condens. Matter* 25, 315402 (2013).

3.10 S. Parker (ISIS), S. Deledda (Institute for Energy Technology, Norway)

3.10.1 Periodic-DFT of a Disordered System: $Mg_2(FeH_6)_{0.5}(CoH_5)_{0.5}$

To enable the widespread use of H_2 as a fuel for automotive applications, a safe, reliable and cheap method for its transportation is essential. A wide variety of materials and approaches have been, and are being, investigated. These include storage: as compressed gas, as physisorbed hydrogen in high surface area porous materials and as chemically bound hydrogen ('chemical hydrogen') such as a metal complex *e.g.* $Mg_2[NiH_4]$ or a hydrogen-in-metal system *e.g.* β -PdH. For storage as chemical hydrogen, ball milling techniques are potentially beneficial for processing hydrogen storage materials. This is a result of the reduction in grain size, that occurs during the continuous fracturing and cold welding of the powder particles and results in improved hydrogen sorption kinetics. Additionally, ball milling can mechanically mix elements and compounds at an atomic scale that may extend the mutual solubility of metals and, in turn, obtain novel materials that may show useful hydrogen storage properties. Ball milling an elemental powder mixture of $Mg_2Fe_{0.5}Co_{0.5}$ in an H_2 atmosphere at 5 MPa results in the novel compound $Mg_2[FeH_6]_{0.5}[CoH_5]_{0.5}$ [1].

The complex has a cubic K_2PtCl_6 -type structure (space group $Fm\bar{3}m$) with a cell parameter of $a \sim 6.42$ Å. The Fe and Co atoms are arbitrarily distributed on the octahedral site (4a) and the magnesium counter-ions are all on the tetrahedral sites (8c). The hydrogen atoms are in an octahedral arrangement around the Fe ion and in a square based pyramid around the Co ion. The $[CoH_5]^+$ complex is randomly oriented in the lattice such that each of the six octahedral vertices has an average occupancy of 5/6. Here we use a combination of inelastic neutron scattering (INS) spectroscopy [2] and periodic density functional theory (periodic-DFT) [3] to further characterise this novel material. While a disordered material such as this would not be a natural choice for a periodic-DFT study we show that it is feasible to obtain useful results and this offers possibilities for other systems.

Figure 22a shows the INS spectrum of $Mg_2[FeH_6]_{0.5}[CoH_5]_{0.5}$ recorded on TOSCA spectra at ISIS. The spectra of the hydride can be summarised as: 0-270 cm^{-1} translational modes of the ions, 270-670 cm^{-1} librational modes of the $[FeH_6]^+$ and $[CoH_5]^+$ ions, 470-1150 cm^{-1} H-M-H bending modes, 1150-1570 cm^{-1} combinations of libration and bend modes and 1570-2100 cm^{-1} M-H stretch modes.

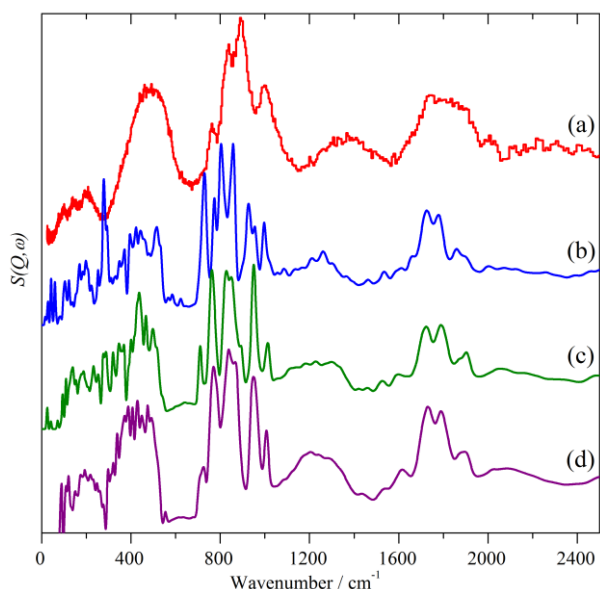


Figure 22: Comparison of the experimental INS spectrum of (a) $Mg_2[FeH_6]_{0.5}[CoH_5]_{0.5}$, with that calculated for (b) the C2v structure for the full dispersion across the Brillouin zone, (c) the 222 structure for the full dispersion across the Brillouin zone and (d) that calculated for the 433 structure at the Γ -point.

Periodic-DFT has been used to successfully model a range of transition metal hydrides [4], in particular, we have extensively used CASTEP on SCARF to study a variety of systems. However, these have all been fully ordered structures. In an initial attempt to extend the use of *ab initio* methods to disordered structures, the $Fm\bar{3}m$ structure of $Mg_2[FeH_6]$ was set to the lattice parameter of $Mg_2[FeH_6]_{0.5}[CoH_5]_{0.5}$ and half the $[FeH_6]^{4-}$ ions changed to $[CoH_5]^{4-}$ ions. This resulted in an ordered structure, space group $Amm2$, of which the primitive cell is shown after geometry optimisation in Figure 23a, (hereafter denoted as the $C2v$ structure). The phonon calculation resulted in three imaginary modes, these are the librations about the crystallographic axes (and would be degenerate in a cubic system). Since these are what would be required to disorder the system, it is unsurprising that they are not real. A comparison of the predicted INS spectrum for the full dispersion across the Brillouin zone is shown in Figure 22b and there is, at best, modest agreement.

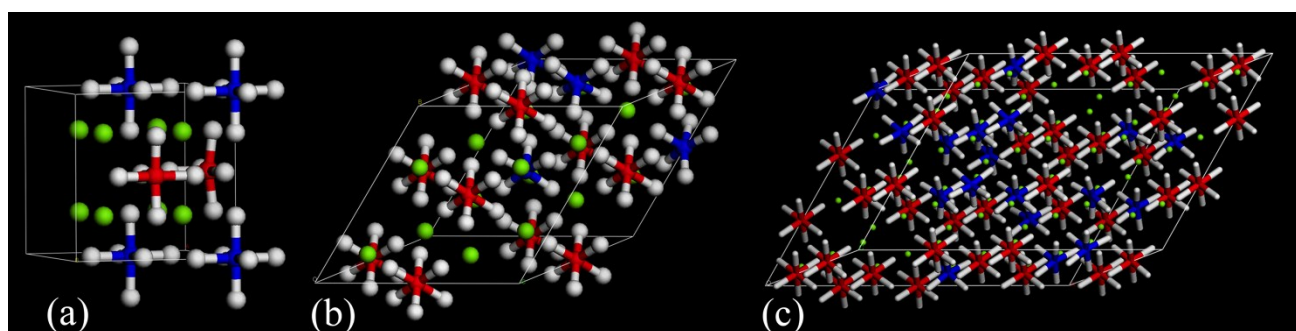


Figure 23: CASTEP geometry optimised structures of $Mg_2[FeH_6]_{0.5}[CoH_5]_{0.5}$: (a) in the ordered space group $Amm2$, (b) and (c) in the disordered cells derived from the $2 \times 2 \times 2$ and $4 \times 3 \times 3$ supercells of the primitive of the $Fm\bar{3}m$ structure of $Mg_2[FeH_6]$ (space groups $P1$). Key: green = Mg, blue = Co, red = Fe, white = H

It is apparent that modelling the disordered system as a structure with a small ordered unit cell is inadequate. To improve the model, a $2 \times 2 \times 2$ supercell of the primitive of the $Fm\bar{3}m$ structure of $Mg_2[FeH_6]$ was constructed at the lattice parameter of $Mg_2[FeH_6]_{0.5}[CoH_5]_{0.5}$. Half of the Fe atoms were then changed to Co and one hydrogen from the resulting ' $[CoH_6]$ ' ion was removed, both procedures were done at random. The resulting structure had $P1$ symmetry and is shown after geometry optimisation in Figure 23b (hereafter denoted as the 222 structure). Figure 22c shows calculated spectrum for the full dispersion across the Brillouin zone. In this case, all the modes were real across the entire Brillouin zone. There is a marked improvement over the results for the $Amm2$ structure, Figure 22b, however, the translational and librational regions are still poorly represented.

As a further extension of the model, the process was repeated using a $4 \times 3 \times 3$ supercell of the primitive of the $Fm\bar{3}m$ structure of $Mg_2[FeH_6]$. The resulting structure had $P1$ symmetry and is shown after geometry optimisation in Figure 23c (hereafter denoted as the 433 structure). Figure 22d shows the comparison between the experimental and the calculated spectra at the Γ -point. Our computational resources did not allow us to carry out the full dispersion calculation (the unit cell contains 306 ions), nonetheless, it can be seen that the agreement is excellent, except that the transition energies are slightly low. (Application of a modest scaling factor of 1.05 produces a calculated spectrum that is almost coincident with the experimental spectrum).

The compound decomposes at a temperature intermediate between the decomposition temperatures of pure $Mg_2[FeH_6]$ and $Mg_2[CoH_5]$, indicating that the $[FeH_6]^{4-}$ anion destabilizes the

$[\text{CoH}_5]^{4-}$ anion and the $[\text{CoH}_5]^{4-}$ stabilizes $[\text{FeH}_6]^{4-}$. The calculations provide an explanation for this effect. In all cases the calculated Co–H distances in the quaternary hydride are shorter than those calculated for $\text{Mg}_2[\text{CoH}_5]$ and the Fe–H distances in the quaternary hydride are longer than those calculated for $\text{Mg}_2[\text{FeH}_6]$. We stress that all the calculations were carried out at the same level of theory, thus the trends are expected to be reliable. Since shorter bonds imply stronger bonds and longer bonds imply weaker bonds, it follows that the M–H bonds in the quaternary hydride of the $[\text{CoH}_5]^{4-}$ and the $[\text{FeH}_6]^{4-}$ ions are stronger and weaker respectively than in the parent compounds, thus the decomposition temperature is intermediate between that of the parent compounds.

The calculations also enable the infrared spectra to be understood. In the mid-infrared spectrum Figure 24a, only the Fe–H and Co–H stretching modes (more clearly seen in the Kramers-Kronig transform, Figure 24b that mitigates the effect of the particle size that causes the derivative-like shape of the band) have any significant intensity, the bending modes are very weak. As far as we are aware, there are no far infrared studies of any ternary metal hydride, however, the calculations show that there is an intense band at $\sim 200 \text{ cm}^{-1}$ assigned to translational modes of the Mg^{2+} and the complex ions, that is almost invariant to deuterium substitution. This is observed at 240 cm^{-1} Figures 24d. The calculations for the parent compounds predict intense modes at similar values, in their cases the modes consist of an antiphase movement of the Mg^{2+} and the complex ions along the Cartesian axes. The CASTEP calculations show that the intensity originates in the large Born charge of the Mg^{2+} ions.

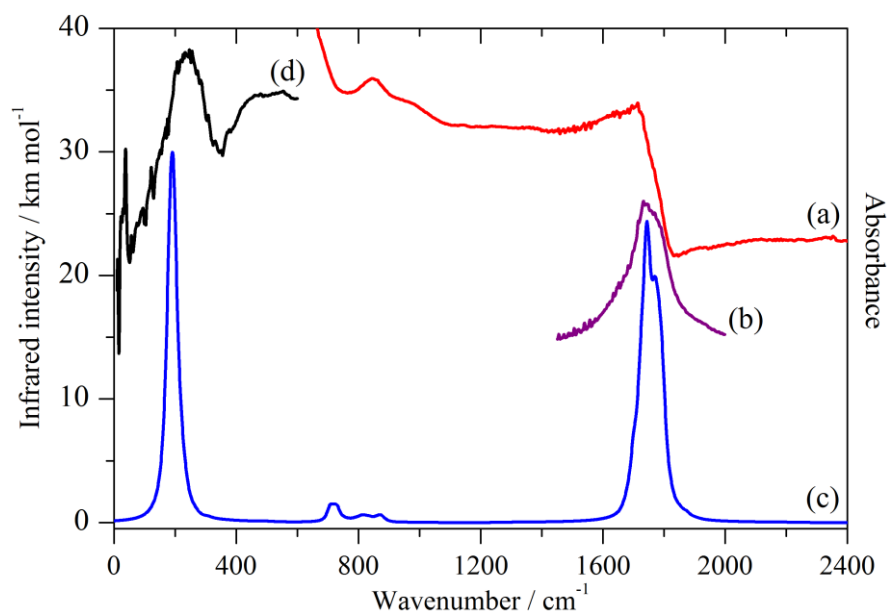


Figure 24: Experimental mid-infrared spectrum of $\text{Mg}_2[\text{FeH}_6]_{0.5}[\text{CoH}_5]_{0.5}$ (a) and after a Kramers-Kronig transformation (b), compared to that calculated for the 433 structure (c). The experimental far infrared spectrum of the compound is shown in (d).

In this work, we have shown that it is possible to characterise a disordered system by periodic-DFT. A modest sized cell is able to capture enough of the disorder present that reliable results can be obtained. Vibrational spectroscopy and *ab initio* calculations are a synergistic pairing: comparison of computed and experimental spectra provides a stringent test of the calculation, while the calculation provides unambiguous assignments of the spectra. The current trend is that the hydrides being synthesised are increasingly complex in order to capture the desired properties. The

approach developed here is potentially applicable to non-stoichiometric hydrogen-in-metal systems, such as the archetypal PdH_x (x = 0 – 1, typically 0.7) or to more complex systems such as YMn₂H_x (x = 0 – 4.3).

[1] Deledda, S.; Hauback, B. C. *Nanotechnology* **2009**, *20*, 204010.

[2] Mitchell, P. C. H.; Parker, S. F.; Ramirez-Cuesta, A. J.; Tomkinson, J. *Vibrational spectroscopy with neutrons, with applications in chemistry, biology, materials science and catalysis* World Scientific, Singapore, 2005.

[3] Clark, S. J.; Segall, M. D.; Pickard, C. J.; Hasnip, P. J.; Probert, M. J.; Refson, K.; Payne, M.C. *Z. Krist.* **2005**, *220*, 567.

[4] Parker, S. F. *Coord. Chem. Rev.* **2010**, *254*, 215-234.

3.11 L. Bernasconi, R. Webster, S. Tomic, B. Montanari and N. M. Harrison (STFC Scientific Computing)

3.11.1 *Electronic excitations and photo-induced dynamics in extended systems*

The *ab initio* description of the optical response of complex extended systems (crystals, glasses, liquid solutions) is currently one of the most active and potentially far reaching subjects of research in electronic structure and condensed matter theory. The Theoretical and Computational Physics group at RAL has devoted a substantial effort in the last few years to develop methods for accurately describing from first principles the optical properties of molecular and crystalline systems, based on extensions of the density-functional formalism to electronically excited states. These new developments pave the way for the accurate prediction of UV-vis, Raman and fluorescence spectroscopy in the solid state, as well as for the study of excited state structure and dynamics and for the simulation of photo-induced chemical processes in complex environments. Excited state capabilities have been implemented in the **CRYSTAL** and **CASTEP** *ab initio* packages, which have both been optimised for parallel execution on SCARF and are available to users through dedicated environment modules.

The CRYSTAL code, in particular, has been optimised to perform excited-state calculations on crystalline systems, and a large component of the application work to date has been carried out on SCARF. This work has been largely devoted to the description of exciton formation in crystals, exciton properties and exciton-lattice interaction. For the first time we have shown that the formation of bound excitons in semiconductors (Wannier-Mott) and wide-gap insulators (Frenkel) can be accurately described using a combination of time-dependent density-functional theory (TD-DFT) and time-dependent Hartree-Fock (TD-HF), [1] with accuracies in theoretical absorption energies of less than 0.1 eV compared to experiment. [2] We have also developed methods for computing exciton binding energies (electron-hole interaction energy) [3, 4] and exciton Rydberg series completely from first principles. [4] These properties are of fundamental relevance for the study of new materials for photo-voltaic energy production and storage, opto-electronics and in the modelling of photo-induced electron transfer processes in biological and biomimetic systems.

Our current work focuses on the study of atomic relaxation following photo-excitation processes in crystals, polymers and liquid solutions. The approach we use combines *ab initio* molecular dynamics and TD-DFT/TD-HF to propagate in real time excited state structures and determine instantaneous or time-averaged properties from dynamical trajectories. These quantities can be used to estimate exciton-phonon coupling, atom-coupled electron transfer parameters and to model *e.g.* fluorescence and transient photo-induced absorption in pump-probe experiments. Current applications are of particular relevance to experimental work carried out by the STFC Facilities, and include the simulation of X-ray and UV induced damage in proteins and DNA (Diamond) and the modelling of laser induced reactivity in anti-oxidant molecules in solution (Central Laser Facility).

[1] L. Bernasconi, R. Webster, S. Tomic, and N. M. Harrison, *Optical response of extended systems from time-dependent Hartree-Fock and time-dependent density-functional theory*, J. Phys.: Conf. Ser. **367**, 012001 (2012)

[2] L. Bernasconi, S. Tomic, M. Ferrero, M. Rerat, R. Orlando, R. Dovesi, and N. M. Harrison, *First principles optical response of semiconductors and oxides*, Phys. Rev. B **83**, 195325 (2011)

[3] S. Tomic, L. Bernasconi, B. Searle and N. M. Harrison, *Optical properties of wurtzite CuInS₂*, in preparation (2013)

[4] R. Wester, L. Bernasconi and N. M. Harrison, *Excitons in alkali halides*, in preparation (2013)

[5] L. Bernasconi and N. M. Harrison, *Hartree-Fock response theory for extended systems*, in preparation (2013)

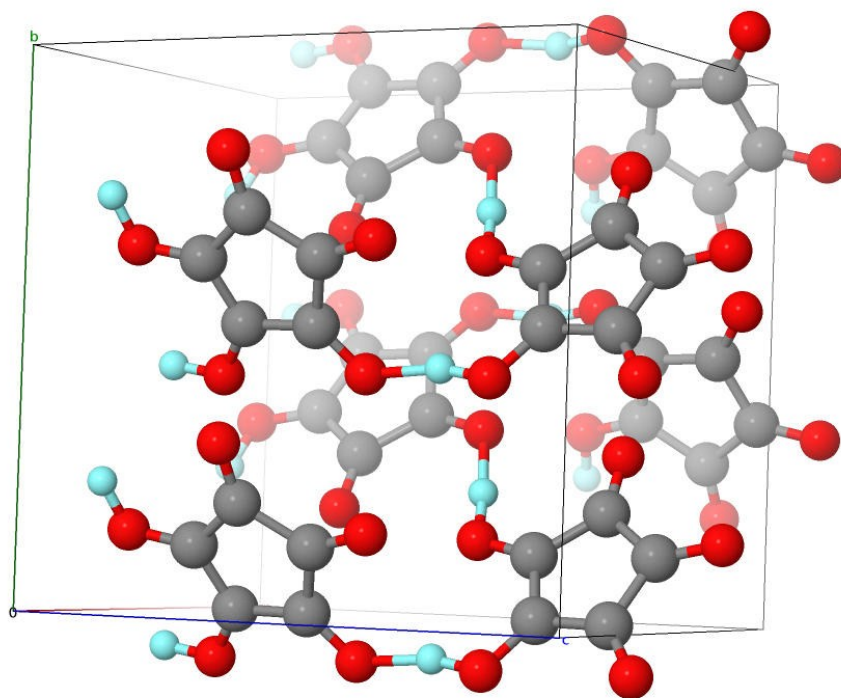
3.12 D. Jochym, S. Sturniolo, and K. Refson (STFC Scientific Computing)

3.12.1 *Ferroelectric Properties of Croconic Acid*

Ferroelectricity is a property of some dielectric materials, which can spontaneously evolve an electric polarization. Such materials have been used to manufacture compact and tunable capacitors, are usually also piezoelectric and pyroelectric, and have been the subject of fundamental materials physics studies ever since their discovery in 1920.

The discovery in 2010 of room-temperature ferroelectric properties in an organic molecular crystal, croconic acid, was a major advance. Until recently, most ferroelectrics have been inorganic salts, (frequently containing expensive or toxic elements) or are ferroelectric only at very low (cryogenic) temperatures. The prospect of easily synthesized and benign organic ferroelectrics which can operate at room temperature opens up possibilities for many new applications, for example in electronics.

In a collaborative project with the ISIS Spectroscopy Group, we have been using the CASTEP quantum mechanical materials simulation code (<http://www.castep.org>) on SCARF to model croconic acid and its cousin, squaric acid. This method is ideally suited to investigate the electronic and atomic structural origins of its anomalous ferroelectric behaviour. It is suspected that the hydrogen-bonding which forms molecular chains and sheets is responsible for its ferroelectric properties and this has been studied experimentally using inelastic neutron scattering and solid-state proton NMR. Our calculations complement and help interpret the INS measurements performed by our ISIS collaborators. First results have already led to two peer-reviewed publications.



Jmol

3.13 B. Montanari and N. M. Harrison (STFC Scientific Computing)

3.13.1 *Surveying Defects in Graphene*

Many proposed applications of graphene require the ability to tune its electronic structure at the nanoscale. The controlled engineering of defects represents a promising approach to the creation of the desired properties. This approach requires control of defect creation at the atomic scale together with the understanding of how defects impact on the properties of the material.

Our long-term programme of work employs first-principles atomistic simulations combined with aberration-corrected transmission electron microscopy (AC-TEM) performed by our collaborators at Oxford University. Defects are created using an electron beam and imaged by AC-TEM with atomic resolution. The simulations are used in two ways: firstly, the microscopy images are simulated to ascertain the underlying atomic structure; the so-determined atomic structure is then used as input for further simulations that determine their electronic and magnetic properties.

This approach leads to the discovery of trends which inform on how to manipulate the structure at the nanoscale so as to instil the wanted properties.

During the last year we have investigated specific defects such as the carbon monovacancy and Fe absorbed over carbon mono- and di-vacancies.

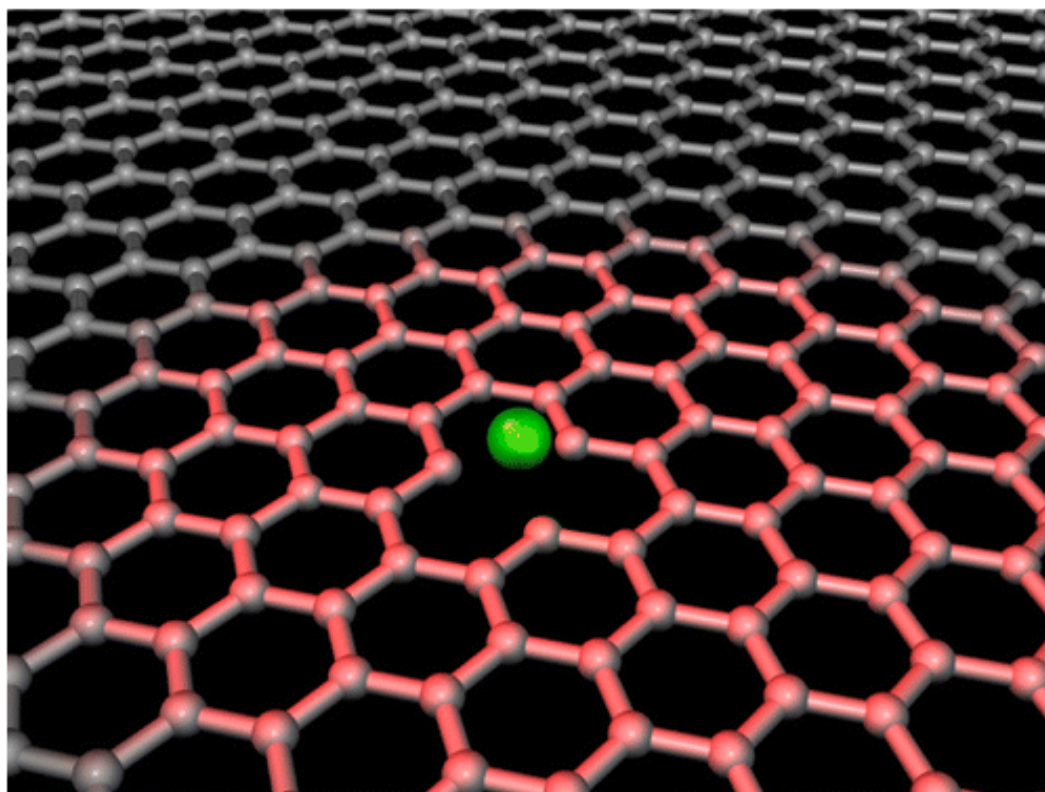


Figure 25: Cartoon of a Fe atom (in green) absorbed over graphene. The red area represents the electron beam used to create and image the defects

3.14 K. Refson (STFC Scientific Computing) and M. Gutmann (ISIS)

3.14.1 Neutron diffuse scattering study of CaTiSiO_5

2013 is the centenary year of the seminal achievement of William and Laurence Bragg who first used X-Ray crystallography to study the atomic structure of crystals, and one of the first topics in any undergraduate course in crystallography today is still Bragg's Law, which holds that almost all of the diffracted intensity of a neutron or X-Ray beam is concentrated in narrow directional rays known as Bragg peaks. But this is not the whole story, and crystallographers have long known that diffracted intensity can also be measured in between the Bragg peaks. This is known as "diffuse scattering" and can arise either from some measure of disorder in the crystal structure or from the thermal vibrations, phonons, of the atoms in the crystal, in which case it is called *thermal diffuse scattering* or TDS. Modern diffraction instruments such as SXD at ISIS, and many X-Ray spectrometers are equipped with expensive area detectors which collect this diffuse scattering, only to discard it, as crystallographic analysis uses only the intensity information at the Bragg peaks.

In a collaborative project between SCD, ISIS and other neutron and X-Ray facilities we have investigated the TDS in single crystals of CaTiSiO_5 . The measurements are compared with the theoretically calculated TDS distribution, based on *ab initio* lattice dynamics (phonon) calculations. These were performed using the CASTEP simulation code on SCARF. The figure shows a comparison of the measured and calculated TDS. The similarity in both the patterns of streaks and spots as well as the shapes of the scattering spots, means that the *ab initio* description of the lattice dynamics is giving a reasonable account of the true phonon dispersion. This provides a stricter test than the usual method of simply comparing frequencies, since the details of the TDS pattern depend strongly on the specific atomic displacements of each phonon mode.

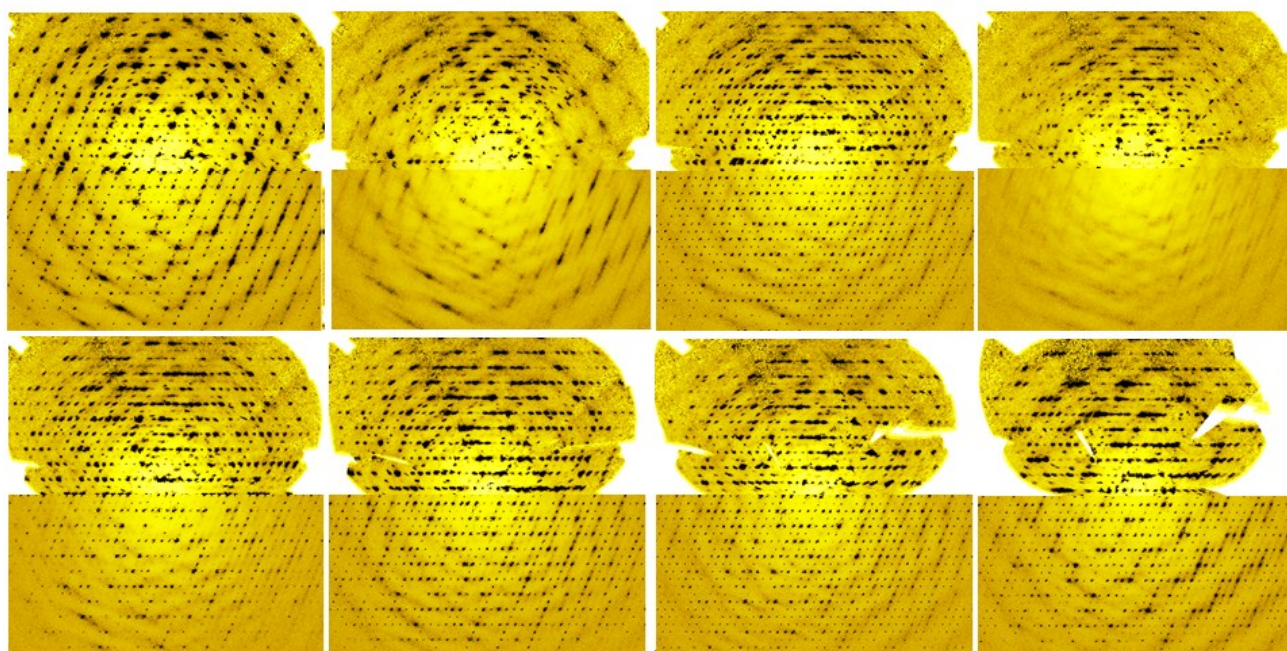


Figure 26: Comparison between observed (upper half in each image) and simulated (lower half) diffuse scattering at 300K in CaTiSiO_5 measured on SXD at ISIS and calculated using CASTEP on SCARF.

3.15 S. Mukhopadhyay (ISIS)

3.15.1 Investigation on Vibrational Modes of Croconic Acid using Inelastic Neutron Scattering

Croconic Acid ($C_5O_5H_2$) is the first single component organic molecule which shows room temperature ferroelectricity in its solid state form [1,2]. In crystalline form, croconic acid molecules are arranged in hydrogen bonded sheets connected through hydrogen bonded hinges. We employed neutron diffraction experiment on SXD at ISIS to understand the crystalline structure of this molecular crystal and inelastic neutron spectroscopy (INS) on LAGRANGE at ILL and on TOSCA at ISIS to understand its vibrational properties. The experimental data were analysed using state-of-the-art calculations based on plane wave pseudo potential density functional theory (DFT) to understand the nature of hydrogen bonds in this material [3,4]. We have used CASTEP code and PBE+D functional for these calculations on SCARF computer.

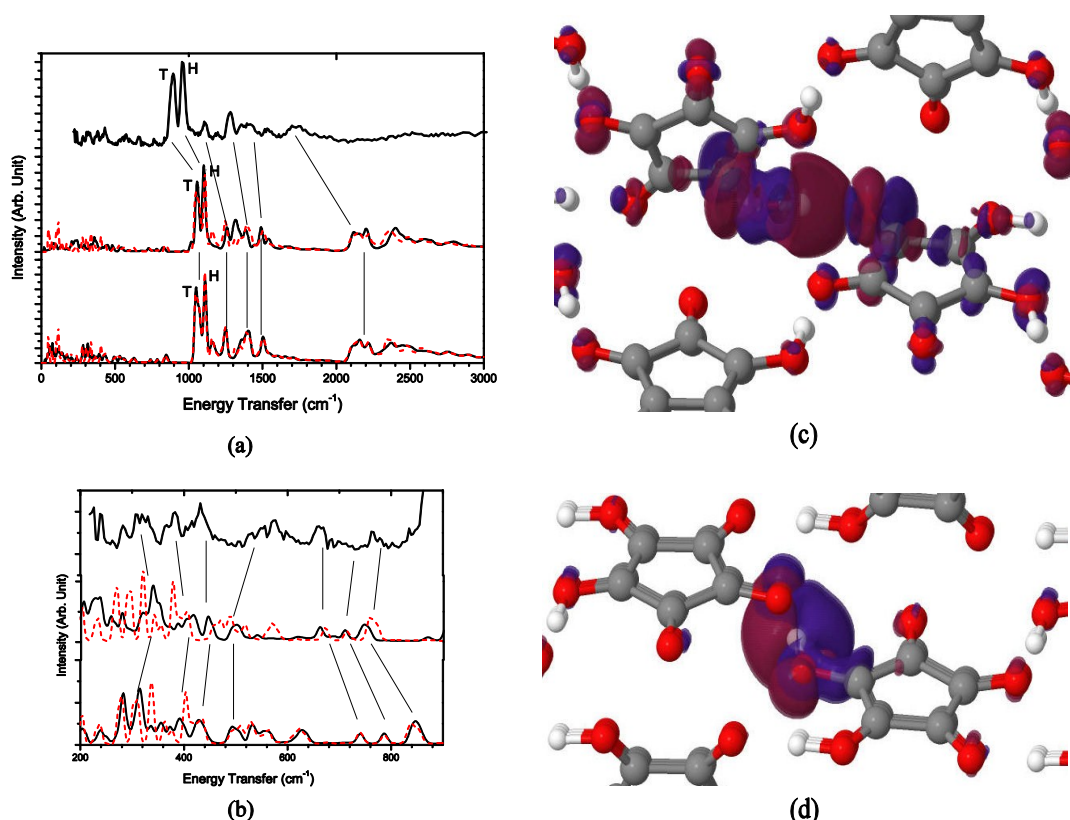


Figure 27: Experimental and calculated INS spectra of solid CA over (a) the whole spectral range; and (b) at low energy transfers; along with the response function at (c) hinge (H) site and (d) terrace (T) site hydrogen bonds. For clarity, the data in (b) are shown in a different intensity scale. On each figure of (a) and (b), the top spectrum corresponds to experimental data whereas the middle and bottom ones are simulated spectra using linear response and finite-displacement methods, respectively.

From this combination of experimental and computational data, we conclude that dispersion-corrections within the GGA approximation (PBE+D) are important for a satisfactory description of the structural properties of solid croconic acid. We also find that once a suitable structural model is determined, other properties such as vibrational band structure appear to be less sensitive to these corrections. We anticipate that this result will be of relevance to future studies of other single-component organic ferroelectrics, particularly in those cases where experimental data remain sparse.

Two distinct vibrational peaks have been identified related to two types of hydrogen bonds present in the solid (See Fig. 27) located at the 'hinge' (H) and 'terrace' (T) positions of a pleated, accordion-like structure of croconic acid. Phonon calculations and simulated neutron spectra show that the prominent doublet observed at ca. 1000 cm⁻¹ arises from out-of-plane motions associated with these two types of hydrogen ions [3]. Calculated Born-effective-charge tensors yield an anomalously high dynamic charge centered on the hydrogen ions at the hinges [4]. We predict that these hydrogen ions has dominant role in the ferroelectric properties of the crystal.

- [1] S. Horiouchi, Y. Tokunaga, G. Giovannetti, S. Picozzi, H. Itoh, R. Shimano, R. Kumai and Y. Tokura "Above-room-temperature ferroelectricity in a single-component molecular crystal", *Nature*, **463**, 789 (2010).
- [2] A. Stroppa, D. D. Sante, S. Horiouchi, Y. Tokura, D. Vanderbilt, S. Picozzi, "Polar distortions in hydrogen-bonded organic ferroelectrics", *Phys. Rev. B*, **84**, 014101 (2011).
- [3] F Fernandez-Alonso, MJ Gutmann, S Mukhopadhyay, DB Jochym, K Refson, M Jura, M Krzystyniak, M Jimenez-Ruiz, A Wagner, "Hydrogen Bonding in the Organic Ferroelectric Croconic Acid: Insights from Experiment and First-principles Modelling" *J. Phys. Soc. Japan*, **82**, SA001, (2013).
- [4] S. Mukhopadhyay, M. J. Gutmann, M. Jura, D. B. Jochym, M. Jimenez-Ruiz, S. Sturniolo, K. Refson, and F. Fernandez-Alonso, "Ferroelectric Behaviour in Solid Croconic Acid using Neutron Scattering and First-principles Density Functional Theory" *Chem Phys*, (2013), (*in press*)

3.16 C.W. Yong (STFC Scientific Computing) and R. Strange (University of Liverpool)

3.16.1 Molecular dynamics of a 'tethered' cytochrome-cupredoxin electron transfer complex

Copper nitrite reductases (CuNiRs) are enzymes that perform the proton-coupled one electron reduction of NO₂ to NO, a key step in the denitrification pathway of the global nitrogen cycle that returns fixed nitrogen to the atmosphere: NO₂ + 2H⁺ + 1e⁻ → NO + H₂O. CuNiRs are trimeric with each subunit consisting of two cupredoxin-like domains, one of which contains a type 1 Cu (T1Cu) site. Located at each trimer intersubunit interface is a type 2 Cu (T2Cu) site. NO₂ binds and is reduced at the T2Cu site, a process that requires electron transfer from the T1Cu site, proton delivery to the T2Cu, and an electron donor redox partner protein, which is a c-type cytochrome (containing Fe-haem) or a cupredoxin (Cu containing). In our previous studies on CuNiRs we proposed a detailed 'ordered' catalytic mechanism [1][2], provided the first experimental evidence for proton coupled electron transfer[3], identified the key amino acid residues involved in entry and delivery of NO₂ to the T2Cu site and mapped out the proton delivery pathways from the protein surface to the catalytic site [4][5].

The interactions between CuNiRs and their individual electron donor proteins are by nature very transient and difficult to capture and the structure of such a complex was reported only recently, for the bacterial CuNiR–Cyt_c551 complex from *Alcaligenes xylosoxidans* [6]. At Liverpool, we have also recently discovered [7] and structurally characterised [8] (figure 28) a variant from *Ralstonia pickettii*. This new family of CuNiRs contains a cytochrome c domain C-terminal extension, representing a 'tethered' electron transfer complex, comprising the Fe-haem and the T1Cu and T2Cu sites contained in separate domains in one protein. The ultra-high resolution (1Å) structure of *R. picketti* CuNiR provides a unique basis for further detailed experimental and computational studies of what is a normally found as a transient electron transfer protein-protein complex.

Our initial work, reported here, has focused on all-atom explicit-solvent molecular dynamics studies. The simulation models were set up using DL_FIELD [9], while simulations were run on Scarf machines up to 128 nodes using DLPOLY_4 program [10]. The aim is to examine the fluidity of the interaction between the cytochrome and cupredoxin domains, Figure 29. The interaction between these two domains must be effective in 'tuning' the electron transfer from the Fe-haem centre to the T1Cu site. The structure shows that water mediated electron transfer is a possible feature of this process and we have employed the TIP5P water model to observe the detailed solvent-diffusion in the channels between the cupredoxin and cytochrome domains.

[1] Strange, R.W. et al *J Mol Biol* **1999**, 287, 1001-1009.

[2] Leferink, N. et al *Biochemistry* **2011**, 50, 4121-4131.

[3] Brenner, S. et al *J Biol Chem* **2009**, 284, 25973–25983.

[4] Antonyuk, S.V. et al *Proc Natl Acad Sci* **2011**, 108, 15780-15785.

[5] Hough, M.A. et al *Biochemistry* **2008**, 47, 13547–13553.

[6] Nojiri, M. et al *Nature* **2009**, 462, 117–121.

[7] Han, C. et al *Biochem J* **2012**, 444, 219–226.

[8] Antonyuk, S.V. et al *Nature* **2013**, 496, 123-126.

[9] C W Yong, *CSE Frontier*, STFC Computational Science and Engineering, R Blake, Ed. Daresbury Laboratory, p38-40 (2010)

[10] I.T. Todorov, W. Smith, K. Trachenko & M.T. Dove, *J. Mater. Chem.*, 16, 1911-1918 (2006)

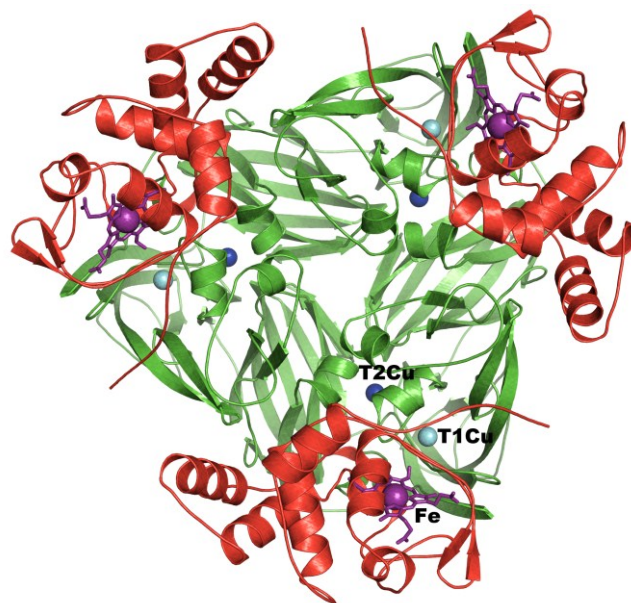


Figure 28: Ribbon diagram of RpNiR trimer⁴, showing the cupredoxin-like domains (green), where T1Cu and T2Cu sites are located and the cytochrome domains (red), where the Fe-haem (purple) are located.

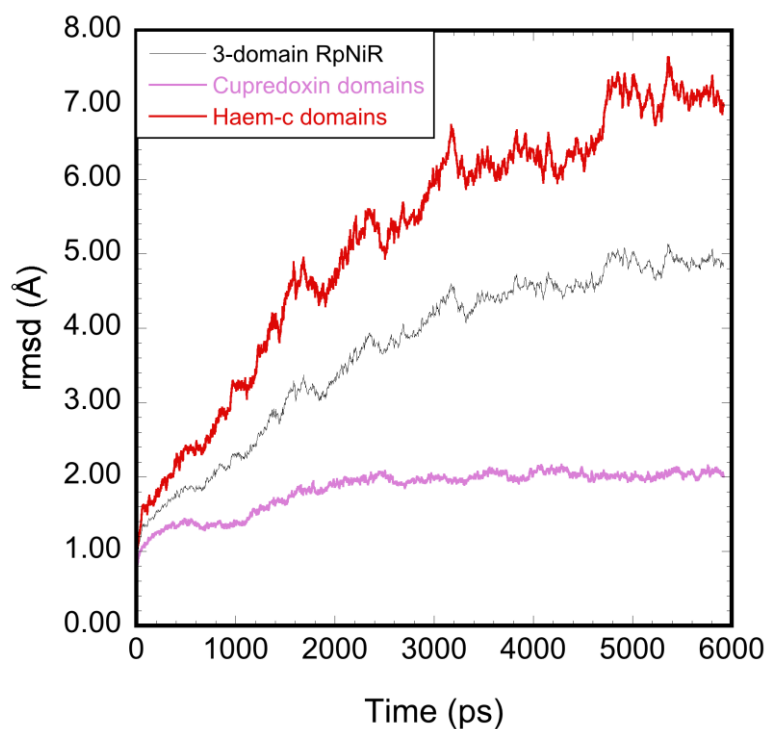


Figure 29: Average root mean-square differences (rmsd) of the cupredoxin domains (pink), cytochrome haem-c domains (red) and the overall variation (black) in the RpNiR trimer, with respect to the X-ray crystal structure, obtained from MD trajectories up to 6ns.

4. APPENDIX: SCARF HARDWARE DETAILS

Host group	CPU type and frequency	Nodes	Cores /node	Total cores	Interconnect	Total memory
SCARF13	Intel E5-2660 @ 2.20GHz	68	16	1088	QDR Infiniband	4352GB
SCARF12	Intel X5675 @ 3.06GHz	20	12	240	QDR Infiniband	960GB
SCARF11	Intel X5660 @ 2.8GHz	32	12	384	QDR Infiniband	768GB
Lexicon-2/ SCARF10	Intel E5530 @ 2.40GHz	104	8	832	DDR Infiniband	2496 GB
IBIS/ SCARF09	Intel E5462 @ 2.80GHz	48	8	384	SDR Infiniband	768 GB
SCARF08	Intel E5430 @ 2.66GHz	46	8	368	SDR Infiniband	736 GB
Lexicon 1 (2013)	Intel E5-2660 @ 2.20GHz	16	16	256	GB Ethernet	1024 GB
Grand Totals		334		3552		11104 GB

5. APPENDIX: INDEX OF FIGURES

Figure 1: Pie chart showing percentage usage of the SCARF service by department 5

Figure 2: Table displaying detailed usage from 2012-13 comparing with 2011-12 and 2010-11 6

Figure 3: Availability for SCARF 6

Figure 4: Availability vs. Year Purchased 7

Figure 5: From left to right the images show a false colour image of the clouds as viewed by the visible channels on the AATSR satellite, the cloud top height (CTH) optical depth (i.e. thickness of the cloud) and effective radius of the particles visible at the top of the cloud. 10

Figure 6: (a) - Zephyros simulation arrangement – ultra-intense laser pulse of intensity I_L and duration τ_L incident at the front surface of a thin, solid density aluminium foil at an angle of θ_L . Resistivity (ρ_{resist}) is calculated by the Lee -More resistivity model, and the fast electron injection angle (θ_e) is a free parameter (b) resulting background temperature viewed from the side of the target, with the laser propagating in the Z direction. (c) Temperature profile as in (b) but viewed at $Z = 5\mu m$ alongside a post-processed image (d) showing the corresponding emission of 1.8keV x-rays. All images are taken at $t = 600fs$ 11

Figure 7: Simulated geometry. Gamma-ray detectors, 2D lead collimators, and sample are illustrated. The neutron beam, water moderator at 293K at a spallation source, was along the z axis [1]. 14

Figure 8: Ratio of counts on detector A and detector B as a function of gamma ray energies for a Cu slab in a Fe matrix placed at -0.2 cm (black) and 0.2 cm (red) offset along x [1]. 15

Figure 9: Simulated PGGA spectra integrated over (a) $200 \div 900 eV$ and (b) $0.025 eV \div 1200 eV$ neutron energies. 15

Figure 10: EGFR EC domain on membrane. A) inactive monomer; B) inactive dimer; C) active dimer. In B) and C), the two monomers are represented in different colours. 17

Figure 11: EGFR IC domain. A) asymmetric dimer; B) symmetric dimer. The two monomers are represented in different colours. 17

Figure 12: Beam loss as a function of ring position and turn number. 18

Figure 13: RMS beam emittances (blue H, red V) plotted against turn number 19

Figure 14: Horizontal, vertical and longitudinal phase space along with real space at turn 2676 19

Figure 15: Poincare map of a single particle over 3000 turns in normalised phase space, where the colour from blue to red represents start to end of the simulation.	19
Figure 16: The EGFR kinase bound to a ligand.	20
Figure 17: Top : Fast electron density in a simulation with a self-generated magnetic elliptical mirror formed by exploiting magnetic field growth at resistivity gradients.	21
Figure 18: Left: Laser intensity distribution for the interaction of an intense (1019 Wcm ⁻²) short (125 fs) laser pulse with a solid target having a long scale length (4 micron). Right: Fourier spectrum of the longitudinal component of the laser electric field.	23
Figure 19: Decomposition of the adsorption energy of molecular hydrogen on the surface of the layered materials obtained with the optB88-vdW functional. The negative values are due to the correlation energy, specifically to the non-local (green bars) and local (purple bars). The positive values refer to the sum of the exchange and the remaining Kohn-Sham energy (blue bars).	26
Figure 20: Previous Page Left: Phonon dispersion relations calculated using the optB88-vdW (red lines) and the LDA (blue lines) functionals at 0K. Previous Page Right: Simulated diffraction pattern for the h0l plane. Above: X-ray diffraction for the h0l patterns obtained with high-energy diffractometer. The experimental diffraction pattern has been obtained using the high-energy X-ray diffractometer at the HASYLAB/DESY in Hamburg.	29
Figure 21: The table in green shows the graphite in-plane (a and b) and out-of-plane (c) lattice constants calculated at 0K using the LDA and the optB88-vdW functionals. In the five last columns the experimental lattice constants as a function of the T are reported. The orange table reports the comparison between the calculated and experimental anisotropic displacement parameters (ADPs). U11 and U22 refers to the in-plane ADPs, U33 to the out-of-plane ADP, and Uiso refers to the total, isotropic displacement. All the experimental data have been collected using the SXD diffractometer at the ISIS Pulsed Neutron and Muon Source.	30
Figure 22: Comparison of the experimental INS spectrum of (a) Mg ₂ [FeH ₆] _{0.5} [CoH ₅] _{0.5} , with that calculated for (b) the C _{2v} structure for the full dispersion across the Brillouin zone, (c) the 222 structure for the full dispersion across the Brillouin zone and (d) that calculated for the 433 structure at the Γ -point.	32
Figure 23: CASTEP geometry optimised structures of Mg ₂ [FeH ₆] _{0.5} [CoH ₅] _{0.5} : (a) in the ordered space group Amm2 , (b) and (c) in the disordered cells derived from the 2 × 2 × 2 and 4 × 3 × 3 supercells of the primitive of the <i>Fm$\bar{3}$m</i> structure of Mg ₂ [FeH ₆] (space groups P1). Key: green = Mg, blue = Co, red = Fe, white = H.	33
Figure 24: Experimental mid-infrared spectrum of Mg ₂ [FeH ₆] _{0.5} [CoH ₅] _{0.5} (a) and after a Kramers-Kronig transformation (b), compared to that calculated for the 433 structure (c). The experimental far infrared spectrum of the compound is shown in (d).	34
Figure 25: Cartoon of a Fe atom (in green) absorbed over graphene. The red area represents the electron beam used to create and image the defects	38
Figure 26: Comparison between observed (upper half in each image) and simulated (lower half) diffuse scattering at 300K in CaTiSiO ₅ measured on SXD at ISIS and calculated using CASTEP on SCARF.	39
Figure 27: Experimental and calculated INS spectra of solid CA over (a) the whole spectral range; and (b) at low energy transfers; along with the response function at (c) hinge (H) site and (d) terrace (T) site hydrogen bonds. For clarity, the data in (b) are shown in a different intensity scale. On each figure of (a) and (b), the top spectrum corresponds to experimental data whereas the middle and bottom ones are simulated spectra using linear response and finite-displacement methods, respectively.	40

Figure 28: Ribbon diagram of RpNiR trimer⁴, showing the cupredoxin-like domains (green), where T1Cu and T2Cu sites are located and the cytochrome domains (red), where the Fe-haem (purple) are located..... 43

Figure 29: Average root mean-square differences (rmsd) of the cupredoxin domains (pink), cytochrome haem-c domains (red) and the overall variation (black) in the RpNiR trimer, with respect to the X-ray crystal structure, obtained from MD trajectories up to 6ns..... 43

Figure 30: SCARF Queue Usage..... 50

Figure 31: SCARF-Lexicon Usage..... 51

Figure 32: SCARF Lexicon-2 Usage..... 51

Figure 33: SCARF-IBIS Usage 52

Figure 34: SCARF Power Usage 52

Figure 35: GFlops/W for SCARF generations of equipment 53

Figure 36: Filespace usage on the Panasas Storage..... 53

Figure 37: SCARF Network Topology..... 54

Figure 38: SCARF08 and SCARF09 Network Traffic..... 54

Figure 39: SCARF10 and Lexicon 2 Network Traffic..... 55

Figure 40: SCARF11 and SCARF12 Network Traffic..... 55

Figure 41: SCARF13 and Lexicon 1 Network Traffic..... 55

Figure 42: SCARF Application Stack 56

6. APPENDIX: PUBLICATIONS AND PRESENTATIONS

#	Reference	Authors
1	Presentation: <i>First Results from CEMS (A)ATSR Hosted processing Pilots</i> . ESA Big Data conference 5-7 June ESA-ESRIN Frascati, Rome Italy	P Kershaw
2	Pub: <i>Localization of inclusions in multiple prompt gamma ray analysis: a feasibility study</i> Journal of Physics: Conference Series (accepted).	A Miceli, G Festa, R Senesi, G Gorini and C. Andreani
3	Pub: <i>Bi-parametric time-energy acquisition Prompt Gamma Activation Analysis (T-PGAA) for Cultural Heritage studies</i> . Fotonica 2013, 15° Convegno Nazionale delle Tecnologie Fotoniche, Milano, 21-23 maggio 2013 - ISBN 9788887237160, ISBN-A 10.978.8887237/160.	G Festa, A Miceli, R Senesi, C Andreani, E Perelli Cippo, G Gorini and R Cattaneo
4	Presentation: Young Researcher Meeting, SISSA, Trieste, June 2013	A Miceli
5	Presentation: International Conference on Neutron Scattering, Edinburgh, July 2013	A Miceli
6	Pub: Phys.Plasmas, 20 , 062704 (2013)	APL Robinson and H Schmitz
7	Pub: Phys.Rev.Lett., 111 , 065002 (2013)	APL Robinson, AV Arefiev, and D Neely
8	Pub: Phys.Plasmas 20 , 043104 (2013)	M Coury et al
9	Pub: Phys.Rev.Lett., 111 , 095001 (2013)	D Maclellan et al
10	Presentation: IoP Spring Conference on Plasma Physics (2013)	H Schmitz and APL Robinson
11	Presentation: Inertial Fusion Science and Applications Conference in Nara, Japan (2013)	A.P.L.Robinson, H.Schmitz, and J.Pasley
12	Presentation: APS/DPP Annual Meeting (November 2012)	R Trines and W Boekee-West
13	Pub: <i>DL_MONTE: A General Purpose Program for Parallel Monte Carlo Simulation</i> . Molecular Simulation. [Online early access]. DOI: 10.1080/08927022.2013.839871 Published Online: Sep 25, 2013.	JA Purton, JC Crabtree and SC Parker
14	Pub: <i>Simulation of the Adsorption and Transport of CO₂ on Faujasite Surfaces</i> . Journal of Physical Chemistry C. [Just Accepted] DOI: 10.1021/jp4053727 Published Online: Oct 1, 2013	JC Crabtree, M Molinari, SC Parker and JA Purton
15	Presentation: <i>Modelling Zeolites for CO₂ Adsorption</i> presented at MRS Fall Meeting 2012, 27 th November 2012, Boston, USA	JC Crabtree, SC. Parker, J Purton and S Perera
16	Presentation: <i>Molecular Modeling of Zeolites for Carbon Dioxide Sequestration</i> at MRS Fall Meeting 2012, 27 th November 2012, Boston, USA.	JC Crabtree, SC Parker, J Purton and S Perera
17	Presentation: <i>Adsorption and Transport of CO₂ at Faujasite Surfaces</i> at CCP5-MDNet meeting, 4 th April 2013, University of Warwick, UK.	JC Crabtree, SC Parker and J Purton
18	Presentation: <i>Adsorption and Transport of CO₂ at Faujasite Surfaces</i> at 9 th European Conference on Computational Chemistry, 2 nd September 2013, Sopron, Hungary	JC Crabtree, SC Parker and J Purton
19	Presentation: <i>Frontiers in Modelling Optical Excitations of Materials</i> Kavli Royal Society International Centre, Chicheley, UK - Invited talk: <i>TD-DFT in solid state and condensed matter theory: Optical response and excited state dynamics in extended systems</i> (September 2013)	L Bernasconi
20	Presentation: 15 th European Conference on the Spectroscopy of Biological Macromolecules, Oxford, UK – Invited talk: <i>Ab initio modelling of electronic excitations in extended systems</i> (August 2013)	L Bernasconi
21	Presentation: UK-CCP9/CECAM-JCMaxwell Workshop, Oxford UK – Invited talk: <i>TD-DFT description of exciton formation and exciton-lattice interaction in extended systems</i> (July 2013)	L Bernasconi
22	Presentation: TD-DFT Conference in Nantes, France – Contributed talk: <i>TD-DFT in the condensed phase: excitons and their interactions with a crystal lattice</i> (April 2013)	L Bernasconi
23	Presentation: <i>Calculation of Optical Properties of Nanostructures from First Principles</i> CECAM-HQ-EPFL, Lausanne, Switzerland – Invited talk: <i>TD-DFT in extended systems: electronic excitations and lattice dynamics</i> (February 2013)	L Bernasconi
24	Presentation: Seminar at University of Turin, Italy – <i>Time-dependent Density-Functional Theory in the CRYSTAL code</i> (March 2013)	L Bernasconi
25	Presentation: Joint ISIS-SCD modelling and simulation workshop, Abingdon, UK – Invited talk: <i>Atomistic simulation of liquids and soft matter</i> (January 2013)	L Bernasconi

SCARF Annual Report 2012-2013

26	Presentation: Royal Society Seminar on Science and technology of silica nanowires, Kavli Royal Society International Centre, Chicheley, UK - Invited talk: <i>Optical properties of amorphous silica nanowires</i> (November 2012)	L Bernasconi
27	Presentation: CCP9 Annual Meeting, University College London, UK - Invited talk: <i>Time-dependent density-functional theory for extended systems</i> (July 2012)	L Bernasconi
28	Presentation: Seminar at Joule Physics Laboratory, University of Salford, UK - <i>First-principles optical response of extended systems from time-dependent density-functional theory</i> (March 2012)	L Bernasconi
29	Presentation: Seminar at Physical and Theoretical Chemistry Laboratory, University of Oxford, UK - <i>TD-DFT and the optical response of extended systems</i> (March 2012)	L Bernasconi
30	Presentation: Theory, Modelling and Computational Methods for Semiconductors Workshop, University of Leeds, UK – Invited talk: <i>First-principles optical response of semiconductors and oxides</i> (January 2011)	L Bernasconi
31	Pub: <i>Optical response of extended systems from time-dependent Hartree-Fock and time-dependent density-functional theory</i> , J. Phys.: Conf. Ser. 367 , 012001 (2012)	L Bernasconi, R Webster, S Tomic, and NM Harrison
32	Pub: <i>First principles optical response of semiconductors and oxides</i> , Phys. Rev. B 83 , 195325 (2011)	L Bernasconi, S Tomic, M Ferrero, M Rerat, R Orlando, R Dovezi, and NM Harrison,
33	Pub: <i>Optical properties of wurtzite CuInS₂</i> , in preparation (2013)	S Tomic, L Bernasconi, B Searle and NM Harrison
34	Pub: <i>Excitons in alkali halides</i> , in preparation (2013)	R Wester, L Bernasconi and NM Harrison
35	Pub: <i>Hartree-Fock response theory for extended systems</i> , in preparation (2013)	L Bernasconi and NM Harrison
36	Pub: J. Phys. Soc. Jpn. Suppl. 82 (2013) " <i>Hydrogen Bonding in the Organic Ferroelectric Croconic Acid: Insights from Experiment and First-Principles Modelling</i> ".	F Fernandez-Alonso, MJ Gutmann, S Mukhopadhyay, DB Jochym, K Refson, M Jura, M. Krzystyniak, M Jiménez-Ruiz and A Wagner
37	Pub: " <i>Ferroelectric Behaviour in Solid Croconic Acid using Neutron Scattering and First-principles Density Functional Theory</i> ". Chemical Physics. (2013).	S Mukhopadhyay et al.
38	Pub: <i>Dynamics of Single Fe Atoms in Graphene Vacancies</i> , Nano letters 13 (4), 1468-1475 (2013)	AW Robertson, B Montanari, K He, J Kim, CS Allen, YA Wu, J Olivier, J Neethling, NM Harrison, AI Kirkland, JH Warner
39	Pub: <i>Structural Reconstruction of the Graphene Monovacancy</i> ACS nano 7 (5), 4495-4502 (2013)	AW Robertson, B Montanari, K He, CS Allen, YA Wu, NM Harrison, AI Kirkland, JH Warner,
40	Presentation: Poster on carbon monovacancy presented at APS March Meeting 2013, Baltimore(USA)	B Montanari
41	Presentation: Invited seminar at London Centre for Nanotechnology (May 2013)	B Montanari
42	Presentation: Invited talk at NanoteC13 conference, Surrey University, (Aug 2013)	B Montanari
43	Pub: <i>Room temperature single-crystal diffuse scattering and ab initio lattice dynamics in CaTiSiO₅</i> . JOURNAL OF PHYSICS CONDENSED MATTER, 25 (31), p.315402.	MJ Gutmann, K Refson et al.
44	Pub: <i>A frontier orbital study with ab initio molecular dynamics of the effects of solvation on chemical reactivity: Solvent-induced orbital control in FeO-activated hydroxylation reactions</i> , J. Am. Chem. Soc. 135 , 8857 (2013)	L Bernasconi and EJ Baerends
45	Pub: <i>Chloride ion solvation: Electronic and structural effects</i> , Phys. Chem. Chem. Phys. 15 , 13169 (2013)	L Ge, L Bernasconi and P Hunt

SCARF Annual Report 2012-2013

46	Pub: 2013. <i>Molecular dynamics investigation of the disordered crystal structure of hexagonal LiBH₄</i> . Physical chemistry chemical physics : PCCP, 15(21), pp.1–21.	PC Aeberhard, K Refson, and WIF David
47	Pub: <i>Experimental evidence for the structural models of Re₂N and Re₂C from micro-Raman spectroscopy</i> . Physical Review B, 86(1), p.014114.	A Friedrich et al.
48	Pub: <i>Optimized effective potential using the Hylleraas variational method</i> . Physical Review B, 85(23), p.235126.	TW Hollins et al.
49	Pub: <i>Comment on "First-principles study of the influence of (110)-oriented strain on the ferroelectric properties of rutile TiO₂."</i> Physical Review B, 88(13), p.136101.	K Refson, et al.
50	Pub: <i>Solid-aqueous equilibrium in the BaSO₄-RaSO₄-H₂O system: first-principles calculations and a thermodynamic assessment</i> . Geochimica et Cosmochimica Acta, 122, pp.398–417.	VL Vinograd et al.
51	Pub: <i>Suppression of thermal conductivity by rattling modes in thermoelectric sodium cobaltate</i> . Nature Materials 12 p1028–1032 (2013)	DJ Voneshen et al.

7. APPENDIX: SCARF QUEUE USAGE 2011-12

Key:

- Red - number of jobs pending
- Green – number of jobs running
- Yellow – number of jobs gathering CPUs so that they can run (large parallel jobs)
- Blue - total number of Jobs (sum of Red, Green, Yellow)

7.1 General SCARF Queue

Open to all SCARF Users with a capacity of ~1400 CPU cores

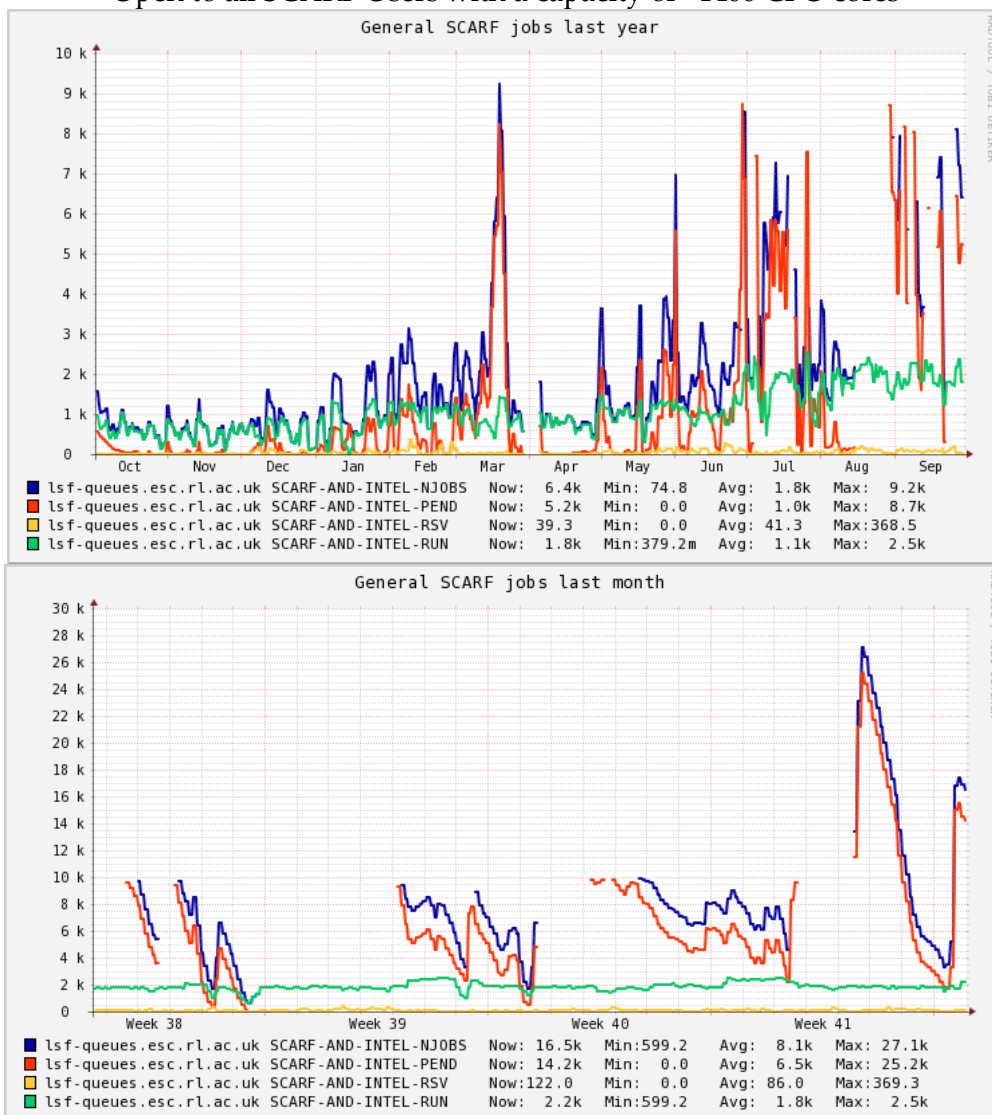


Figure 30: SCARF Queue Usage

The graph for the SCARF queue (and thus the combined SCARF/INTEL graph) shows consistently pending jobs for most of the year, which demonstrates that there is not sufficient capacity. This should be addressed by the next hardware procurement. The number of pending jobs has

significantly increased recently, revealing a limit in our data-gathering where values greater than 10000 were omitted, this limit has now been removed.

7.2 SCARF-Lexicon1 and Lexicon2 Queues

These queues are primarily for CLF use with a capacity of 256 and 544 CPU cores for SCARF Lexicon 1 & 2 respectively. The original 292 cores of Lexicon 1 were replaced this year with 256 new cores in June 2013.

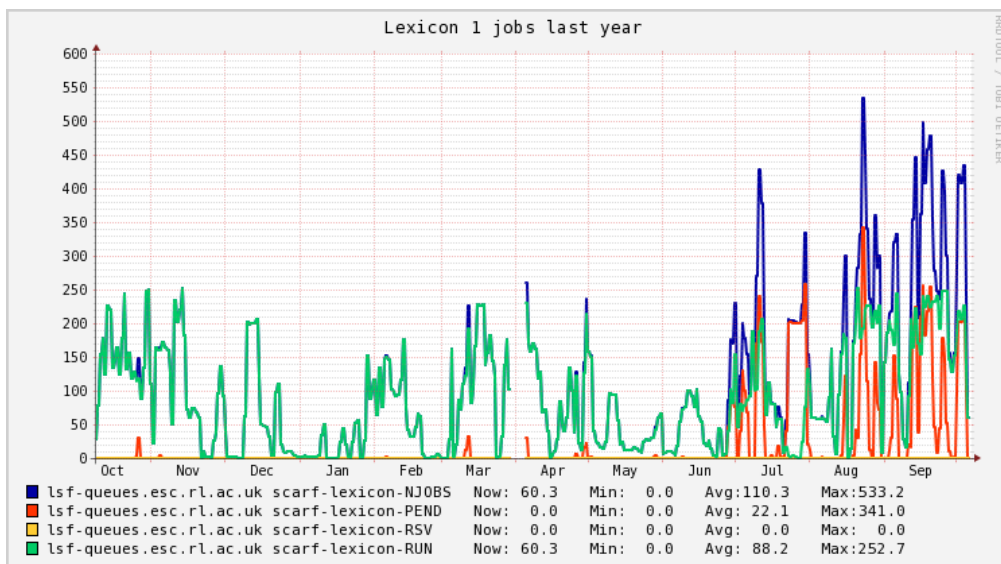


Figure 31: SCARF-Lexicon Usage

The graph for the SCARF-LEXICON queue shows peaky but significant usage, though this has dropped somewhat since the purchase of SCARF-LEXICON-2. The replacement of the original Lexicon 1 systems in June 2013 has coincided with an increase in demand.

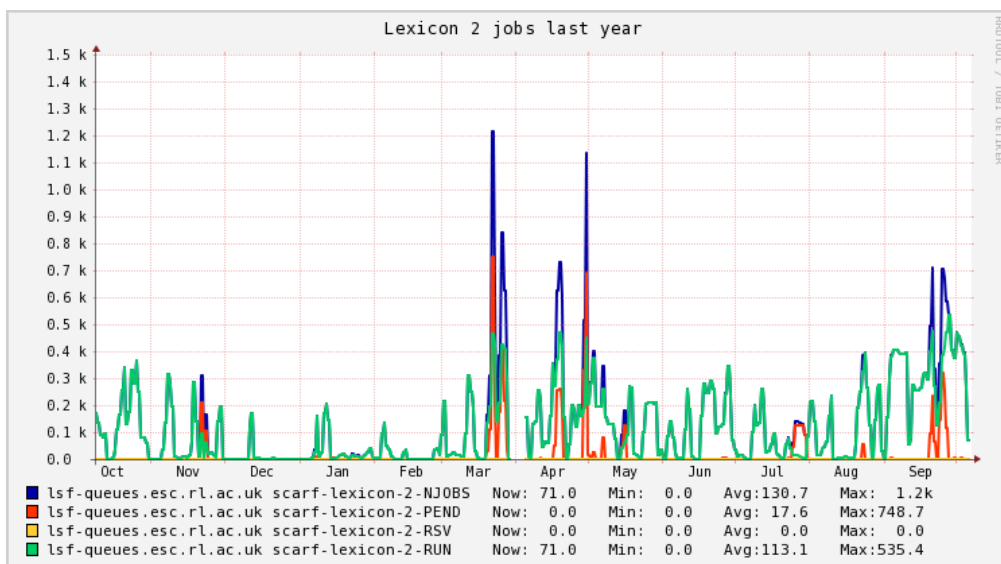


Figure 32: SCARF Lexicon-2 Usage

SCARF-LEXICON-2 continues to be used for higher priority Lexicon users and on demand to support CLF experiments.

7.3 SCARF-IBIS

SCARF-IBIS has a capacity of 144 CPU cores.

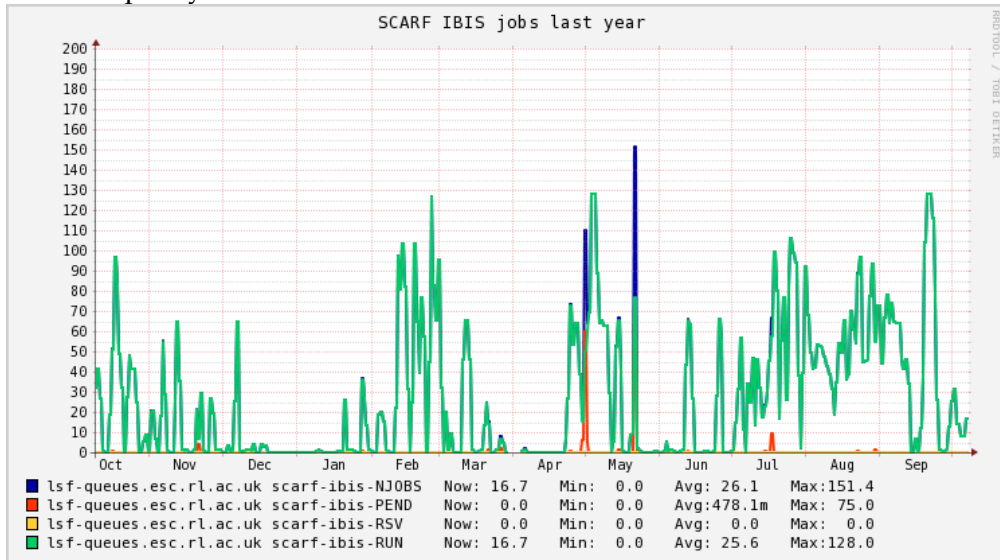


Figure 33: SCARF-IBIS Usage

7.4 SCARF Total Power draw (amps)

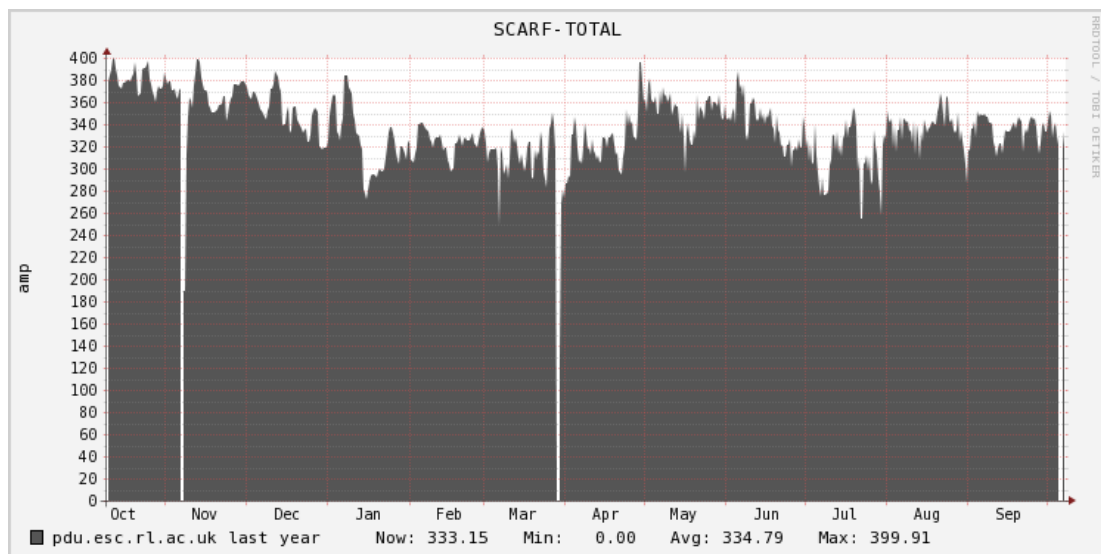


Figure 34: SCARF Power Usage

The approximate average power draw of the SCARF cluster (including Lexicon) is about 335 amps or 80kW. This excludes the power needed to cool, pump and move cold air. The efficiency of SCARF in terms in Gflops/W is giving in the table below.

Year Purchased	Gflops/W
2007	0.09
2008	0.21
2009	0.29
2010	0.32

2011	0.48
2012	0.50
2013	0.59

Figure 35: GFlops/W for SCARF generations of equipment

From the above table it is clear that the GFlops/W achieved increase per generation of the SCARF equipment. This supports the continual refresh rate of SCARF hardware rather than a big bang approach.

7.5 Filesystem Usage

The plot below outlines the use of the Panasas filesystem on the SCARF service. The filesystem is shared across a number of projects therefore not all space is available to SCARF users, but SCARF users benefit as increasing the amount of space also increases the bandwidth to the storage as file are redistributed around the Panasas system automatically.

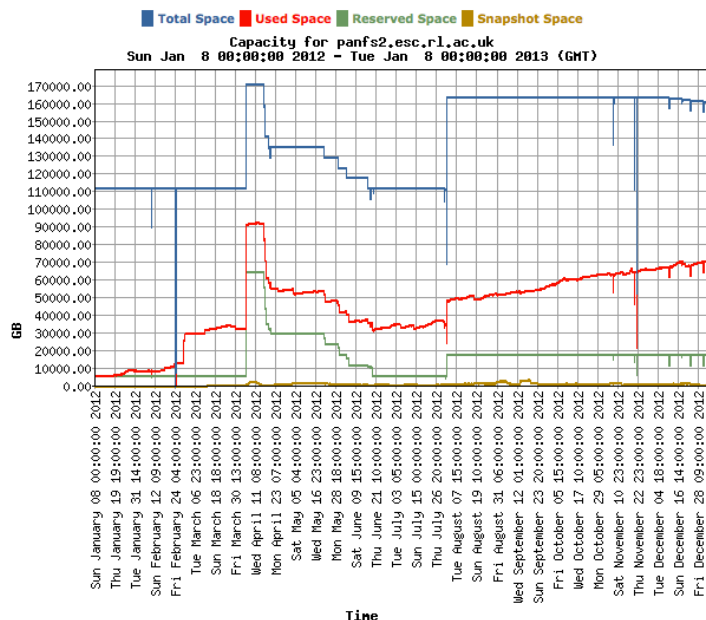


Figure 36: Filespace usage on the Panasas Storage

7.6 Networking

The diagram below shows the SCARF compute clusters embedded in the larger Research Infrastructure group’s networking infrastructure.

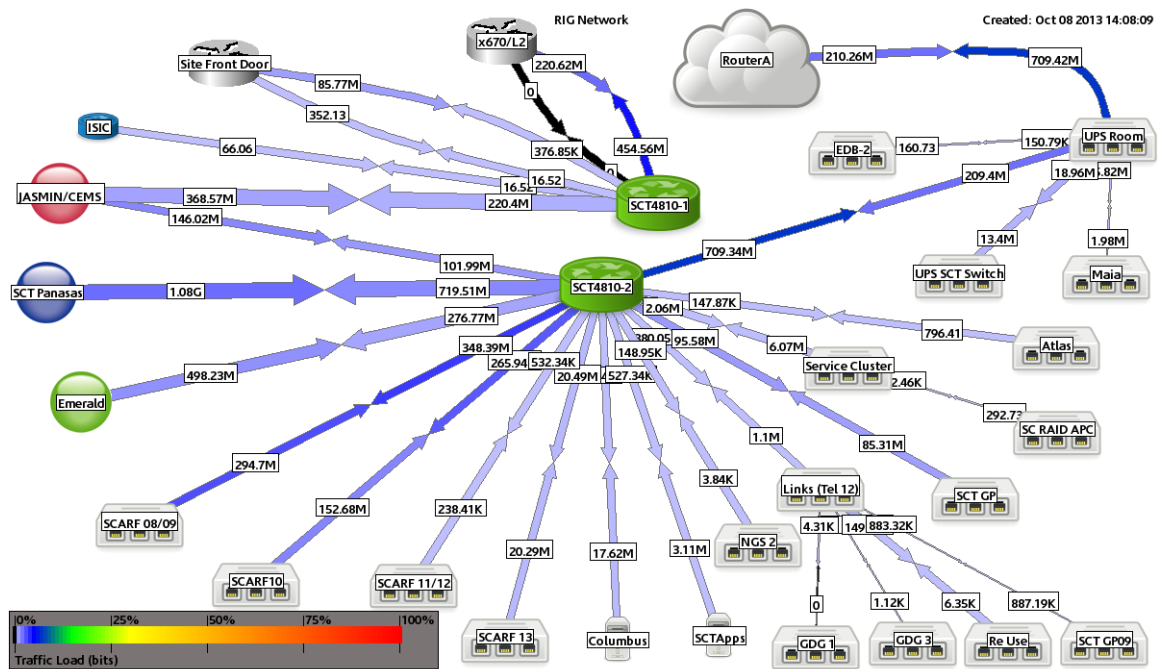


Figure 37: SCARF Network Topology

The following graphs outline the network traffic from the clusters. This captures traffic to the Panasas filesystems, backups and external traffic.

SCARF08 and SCARF09 were originally connected via network switches in the Lexicon 1 racks, but with the decommissioning of that hardware are now connected directly.

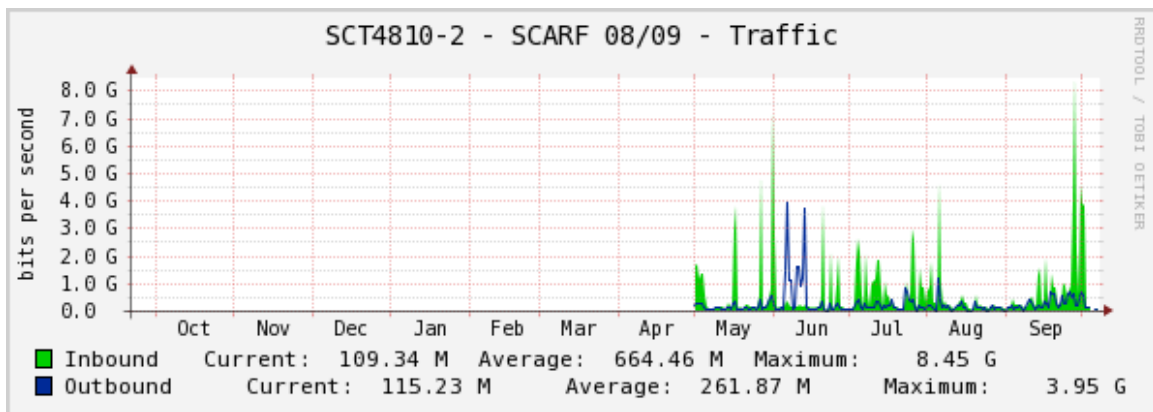


Figure 38: SCARF08 and SCARF09 Network Traffic

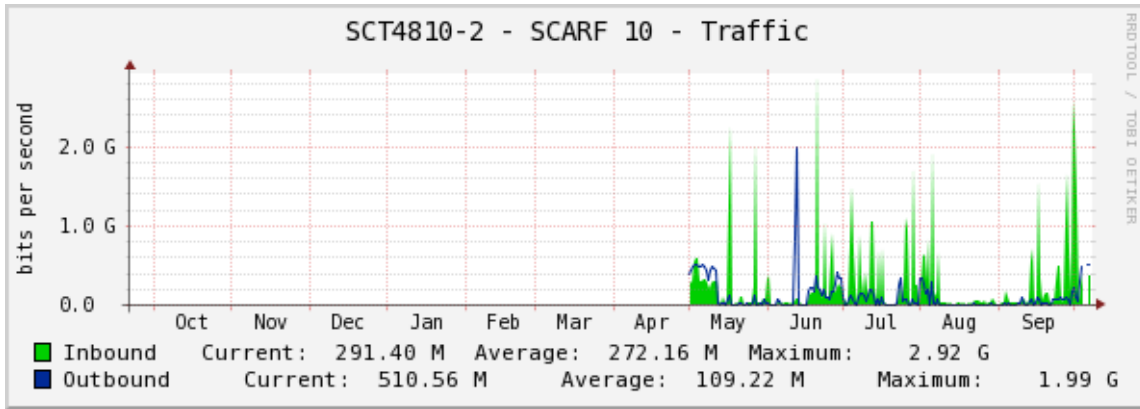


Figure 39: SCARF10 and Lexicon 2 Network Traffic

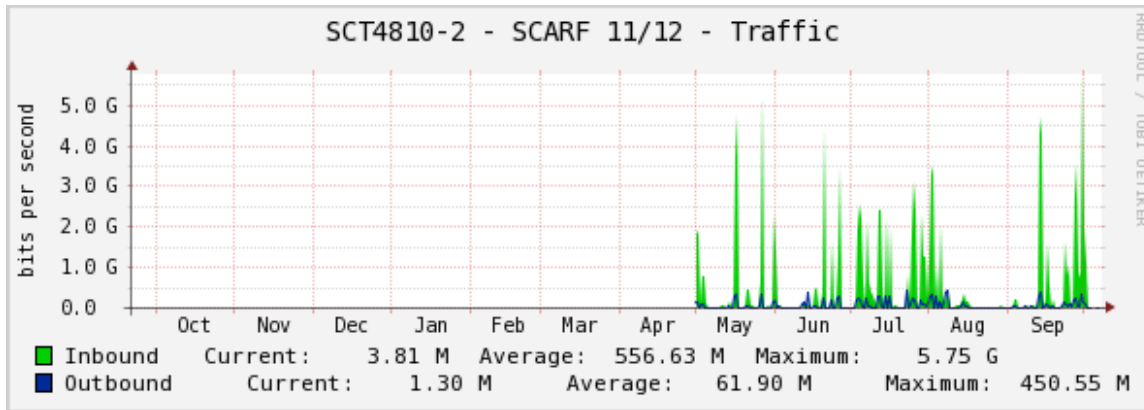


Figure 40: SCARF11 and SCARF12 Network Traffic

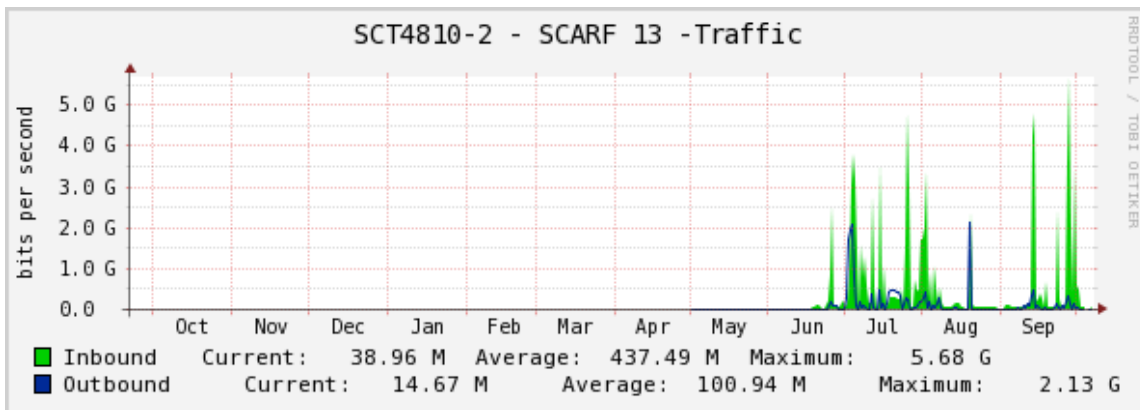


Figure 41: SCARF13 and Lexicon 1 Network Traffic

8. APPENDIX: SCARF DEVELOPMENTS

It has been a busy year for the SCARF service. Users' will have noticed most impact with the additional of capacity and upgrades to applications. However, a lot of effort goes into improving the management of SCARF.

8.1 Technical Developments

- In late June the 2013 hardware tranche of 68 dual Intel E5-2660, providing 1088 cores was made available
- Also in late June the original Lexicon 1 cluster of 292 cores was replaced with 256 cores identical to the 2013 hardware purchase. The original Lexicon 1 cluster has been powered off
- The SCARF06 hardware has been decommissioned and disposed of.
- SCARF now has access to the CEDA archive hosted in R89
- Two new additional work areas were added for CLF and RAL Space to reduce pressure on the existing work area.
- The login and authentication process has been streamlined to make it more robust

8.2 Application Stack

New or updated applications are in the table below:

Application	Area	Version
IDL	Data visualisation	8.2
CASTEP	Computational Chemistry	6.1.1
AMBER	Computational Chemistry	12
CRYSTAL	Computational Chemistry	CRYSTAL09
netCDF	data model, library, and file format for storing and managing data	4.2
ROOT	Particle Physics	5.34.04
Intel compiler	Fortran, C, C++ compilers and Maths libraries	13.1
PGI compilers	Fortran, C, C++ compilers and Maths libraries	13.7

Figure 42: SCARF Application Stack

8.3 Staff Movements

E-Science has merged with the Computational Science and Engineering Department to form a new department: Scientific Computing. As part of that reorganisation the Scientific Computing Technology Group in E-Science, responsible for SCARF, was renamed Research Infrastructure Group. Peter Oliver, group leader of the Scientific Computing Technology Group, has been promoted to head of the Technology Division of Scientific Computing and is no longer involved in the management of SCARF. Nick Hill was promoted to group leader of the Research Infrastructures Group.